

Decomposition contact response (DCR) for explicit finite element dynamics

Fehmi Cirak^{1,*},[†] and Matthew West^{2,‡}

¹*Center for Advanced Computing Research, California Institute of Technology, Mail Code 158-79, Pasadena, CA 91125, U.S.A.*

²*Department of Aeronautics and Astronautics, Stanford University, Stanford, CA 94305, U.S.A.*

SUMMARY

We propose a new explicit contact algorithm for finite element discretized solids and shells with smooth and non-smooth geometries. The equations of motion are integrated in time with a predictor-corrector-type algorithm. After each predictor step, the impenetrability constraints and the exchange of momenta between the impacting bodies are considered and enforced independently. The geometrically inadmissible penetrations are removed using closest point projections or similar updates. Penetration is measured using the signed volume of intersection described by the contacting surface elements, which is well-defined for both smooth and non-smooth geometries. For computing the instantaneous velocity changes that occur during the impact event, we introduce the decomposition contact response method. This enables the closed-form solution of the jump equations at impact, and applies to non-frictional as well as frictional contact, as exemplified by the Coulomb frictional model. The overall algorithm has excellent momentum and energy conservation characteristics, as several numerical examples demonstrate. Copyright © 2005 John Wiley & Sons, Ltd.

KEY WORDS: contact; impact; non-smooth mechanics; explicit dynamics; shells

1. INTRODUCTION

Finite element computations of the dynamic impact and contact of interacting bodies are notoriously difficult, due to the strong non-linearity and non-smoothness of the associated equations. The inherent difficulties in simulating contact have motivated a number of approaches for contact enforcement. Examples are penalty methods [1, 2], which allow penetration to occur

*Correspondence to: Fehmi Cirak, Center for Advanced Computing Research, California Institute of Technology, Mail Code 158-79, Pasadena, CA 91125, U.S.A.

[†]E-mail: cirak@cacr.caltech.edu

[‡]E-mail: westm@stanford.edu

Contract/grant sponsor: DoE; contract/grant number: DOE W-7405-ENG-48, B523297

Received 23 February 2004

Revised 19 July 2004

Accepted 2 March 2005

but penalize it by applying surface contact force models, and exact or approximate Lagrange-multiplier methods [3–6] which exactly preserve the non-interpenetration constraint. In the case of penalty methods, in addition to their fundamental convergence difficulties [5], their sensitivity to the choice of the parameter is often troublesome. While the proper enforcement of the non-interpenetration constraint requires a high penalty parameter, the system becomes increasingly stiff as the penalty parameter is increased. This makes it very challenging for such algorithms to simulate contact when complex geometries require strong enforcement of the contact constraints, such as in crumpling of thin-shells or contact within fragment clusters. Lagrange multiplier methods, on the other hand, typically exactly enforce the contact constraints and so apply in a straight-forward manner to complex settings. However, these methods require the solution of implicit augmented systems of equations, which can become computationally very expensive for large problems. Their implicit character also makes the parallel implementation of such methods very challenging. Further discussion of these and other standard contact algorithms may be found in standard textbooks [7–9].

The explicit contact-enforcement method developed in this paper, termed decomposition contact response (DCR), circumvents a number of the above-mentioned difficulties inherent to conventional contact-enforcement techniques. In the DCR method the enforcement of the impenetrability constraint and the exchange of the momenta during the impact are considered separately. The impenetrability is enforced by means of closest point projections or similar techniques, while the transfer of momentum is accomplished by applying self-equilibrating impulses to the nodes participating in the impact. An important feature of the DCR is its applicability to any properly defined constraint function, such as the gap function or the intersection volume. For example, the constraint function defined as the intersection volume is crucial for the contact of non-smooth bodies in three-dimensional problems. In addition, the DCR method is fully explicit, while still exactly preserving the non-interpenetration constraint at each time-step.

The self-equilibrating impulses applied to the system during the contact event are derived using the non-smooth variational mechanics framework [10, 11]. The applied impulses due to an elastic collision preserve the kinetic energy and all momenta of the system, while the impulses due to friction lead to energy dissipation, but do not change the total linear or angular momenta of the system. In contrast to conventional contact enforcement algorithms, the magnitude of the impulses do not depend on the amount of the penetration, which is a manifestation of the time-discretized system and not the true continuous problem. In particular, for frictional contact the tangential forces should directly depend only on the normal pressures and any non-physical assumptions about the normal pressures may easily harm the fidelity of the numerical solution.

The inputs for the DCR algorithm are the surface finite elements (faces) of the discrete contact surface, independent of the particular features of the finite elements used for discretizing the domain integrals and the material models. Thus, the derived algorithm can be used for shells or solids and facilitates the implementation of modular software packages, which is critical for concurrent multi-scale and multi-physics finite element codes, such as described in Reference [12]. Further, to simplify the algorithmic implementation we specialized the DCR method to the treatment of pairwise collision of the contact surface elements. The two possible penetration scenarios for two contact surface elements embedded in three-dimensional space are node–face and edge–edge contacts. Although in many applications the treatment of node–face penetrations is sufficient, for situations such as those involving impact between non-smooth bodies, the proper consideration of edge–edge contact is crucial. The contact constraints are

only enforced at the end of each time-step. Therefore, pairwise treatment of collisions may lead to ambiguities, since some elements or nodes may participate at several collisions. To strictly enforce causality it is necessary to prioritize the collision events with respect to the collision times. However, in the numerical computations the overall response of the colliding bodies is only slightly influenced by the order of the collision events within a time-step.

The final integration method developed in this paper can be regarded as an efficient, explicit approximation to the implicit rigid-body impact method developed in Reference [11] using the framework of variational non-smooth mechanics. Previous work within the conceptual framework includes [13, 14]. In these papers the contact enforcement is of implicit type and formulated as a non-linear constrained optimization problem. For large-scale problems, the efficiency of the explicit overall time-integration scheme is adversely affected by the implicit contact enforcement algorithm. As well known, in applications with high-velocity gradients and frequencies close to the natural frequency of the material, explicit-type contact enforcement and time-integration schemes are in general more efficient.

The paper begins in Section 2 by stating the equations of motion for a finite element discretization of a contact-impact problem, and then describes the basic DCR time-discretization strategy in Section 3. The key element of the DCR method is the efficient calculation of the impulses produced by contact, based on linear decompositions of the momenta. This is described in Section 4, and illustrated with a number of simple examples in Section 5. The practical performance of the DCR method is then demonstrated on a number of numerical examples in Section 6. Finally, the momentum decompositions necessary for the DCR method are derived for general geometries in Section 7.

2. DISCRETE IMPACT EQUATIONS

In the following we briefly review the derivation of the variationally consistent discrete impact equations for finite-dimensional systems, such as those for a finite element discretization of a hyperelastic solid or a shell. The derivations are independent of the contact constraint definition and essentially independent of the finite elements used. For more details on non-smooth Lagrangian mechanics and the underlying geometrical framework we refer to References [10, 11, 15] and Section 7.

Finite element discretization of a hyperelastic solid or shell with a single impact event leads to an action integral of the form

$$S(\mathbf{x}, \dot{\mathbf{x}}, t_c) = \int_0^{t_c} L(\mathbf{x}, \dot{\mathbf{x}}) dt + \int_{t_c}^T L(\mathbf{x}, \dot{\mathbf{x}}) dt \quad (1)$$

where t_c is the unknown impact time and L is the semi-discrete Lagrangian,

$$L(\mathbf{x}, \dot{\mathbf{x}}) = \dot{\mathbf{x}}^T \mathbf{M} \dot{\mathbf{x}} - W(\mathbf{x}) + \mathbf{f}^{\text{ext}} \cdot \mathbf{x} \quad (2)$$

Here \mathbf{M} is the mass matrix, W is the internal energy, \mathbf{x} are the deformed nodal positions, $\dot{\mathbf{x}}$ are the nodal velocities, and \mathbf{f}^{ext} is the external force vector. In the case of multiple impact events over the time interval $[0, T]$, the action is the total sum of the actions between the distinct impact times. In addition, the action integral is augmented by proper boundary and initial conditions for the nodal positions and velocities, which have been omitted here for brevity.

In the presence of contact the geometrically admissible set of deformations $\mathbf{x} \in Q$ are constrained to $\mathbf{x} \in A \subset Q$ with

$$A = \{\mathbf{x} \in Q \mid g(\mathbf{x}) \leq 0\} \tag{3}$$

The constraint function $g(\mathbf{x})$ only depends on the deformed nodal positions and will later be used for enforcing the impenetrability condition. The boundary ∂A , given by $g(\mathbf{x}) = 0$, consists of those deformations for which contact has just occurred without a penetration. Different choices for the constraint function g are possible, such as the gap function or the intersection volume. A detailed discussion of constraint functions is given in Section 3. Note that the (non-unit) normal to ∂A is given by $\nabla g(\mathbf{x})$.

At the equilibrium configurations the action integral is required to be stationary, which is

$$\delta S(\mathbf{x}, \dot{\mathbf{x}}, t_c) = \frac{\partial S}{\partial \mathbf{x}} \cdot \delta \mathbf{x} + \frac{\partial S}{\partial \dot{\mathbf{x}}} \cdot \delta \dot{\mathbf{x}} + \frac{\partial S}{\partial t_c} \delta t_c = 0 \tag{4}$$

Applying standard variational calculus leads to

$$\begin{aligned} \delta S(\mathbf{x}, \dot{\mathbf{x}}, t_c) &= \delta \left(\int_0^{t_c} L(\mathbf{x}, \dot{\mathbf{x}}) dt + \int_{t_c}^T L(\mathbf{x}, \dot{\mathbf{x}}) dt \right) \\ &= \int_0^T \left(\frac{\partial L}{\partial \mathbf{x}} - \frac{d}{dt} \frac{\partial L}{\partial \dot{\mathbf{x}}} \right) \cdot \delta \mathbf{x} dt - \left[\frac{\partial L}{\partial \dot{\mathbf{x}}} \cdot \delta \mathbf{x} + L \delta t_c \right]_{t_c^-}^{t_c^+} = 0 \end{aligned} \tag{5}$$

The first integral in the preceding equation gives the equations of motion to be

$$\mathbf{M}\ddot{\mathbf{x}}(t) + \frac{\partial W(\mathbf{x}(t))}{\partial \mathbf{x}} = \mathbf{f}^{\text{ext}}(t) \tag{6}$$

The geometrical impenetrability condition

$$\delta g[\mathbf{x}(t_c)] = \nabla g \cdot (\delta \mathbf{x}(t_c) + \dot{\mathbf{x}}(t_c) \delta t_c) = 0 \tag{7}$$

is satisfied for two independent combinations of virtual deformations and impact-time variations, namely

$$\delta \mathbf{x} = -\dot{\mathbf{x}}(t_c) \delta t_c \tag{8a}$$

$$\delta \mathbf{x} \cdot \nabla g = 0 \quad \text{for } \delta t_c = 0 \tag{8b}$$

Note that any linear combination of these two constraints also satisfies Equation (7), and indeed that these two possibilities span the set of allowable impact variations. The first equation (8a) inserted in the last term of Equation (5) leads to

$$\left[\frac{\partial L}{\partial \dot{\mathbf{x}}} \cdot \dot{\mathbf{x}} - L \right]_{t_c^-}^{t_c^+} = 0 \tag{9}$$

Similarly, the second equation (8b) introduced in the last term of Equation (5) leads to

$$\left[\frac{\partial L}{\partial \dot{\mathbf{x}}} \cdot \delta \mathbf{x} \right]_{t_c^-}^{t_c^+} = 0 \quad \text{for all } \delta \mathbf{x} \text{ such that } \delta \mathbf{x} \cdot \nabla g = 0$$

which implies

$$\left[\frac{\delta L}{\delta \dot{\mathbf{x}}} \right]_{t_c^-}^{t_c^+} = \lambda \nabla g \quad (10)$$

where $\lambda \in \mathbb{R}$ is a scalar parameter. For the Lagrangian defined in Equation (2) the impact Equations (10) and (9) reduce to

$$[\mathbf{p}]_{t_c^-}^{t_c^+} = \lambda \nabla g \quad (11a)$$

$$[\mathbf{p}^T \mathbf{M}^{-1} \mathbf{p}]_{t_c^-}^{t_c^+} = 0 \quad (11b)$$

where $\mathbf{p} = \mathbf{M}\dot{\mathbf{x}}$ is the momentum vector. From the first equation (11a) follows that only the momentum components in the direction of the normal ∇g change during the impact. The energy conservation for the elastic impact process is described by the second equation (11b). If the momentum $\mathbf{p}(t_c^-)$ immediately prior to the impact event is known, Equations (11a) and (11b) may be used to compute the momentum $\mathbf{p}(t_c^+)$ just after the impact. The resulting momentum conserves the kinetic energy as well as the total linear and angular momenta.

3. TIME DISCRETIZATION

The semi-discrete action integral (1) is discretized by subdividing the time $[0, T]$ into subintervals $0 = t_0 < t_1 < \dots < t_n = T$ and using proper shape functions in time for the deformations and velocities. Following this approach a class of variationally consistent time-integration schemes can be derived [10], including well-known schemes such as the Newmark method [16, 17], which are traditionally derived starting from the semi-discrete equations of motion (6). In our numerical computations we use a scheme equivalent to the explicit Newmark scheme in the predictor-corrector form ($\beta = 0, \gamma = 1/2$).

The motion of the nodal positions resulting from the time-integration of the equations of motion may lead to impacts between discretized surface elements. The discrete impact events lead to jumps in the momenta and velocities of the participating nodes, which are described by the impact equations. In order to solve the impact equations it is necessary to provide the nodal positions and velocities immediately prior to the impact time t_c^- . Since the impacts mostly happen within a time-step $t_{i-1} < t_c < t_i$, a correct treatment of the impact event requires the time-integration of the equations of motion during the intervals $[t_{i-1} < t_c^-]$ and $[t_c^+ < t_i]$ and the solution of the impact equations at the time t_c . Although conceptually straightforward, the described approach is not feasible for finite element discretized systems due to the enormous number of possible impact events during a time-step.

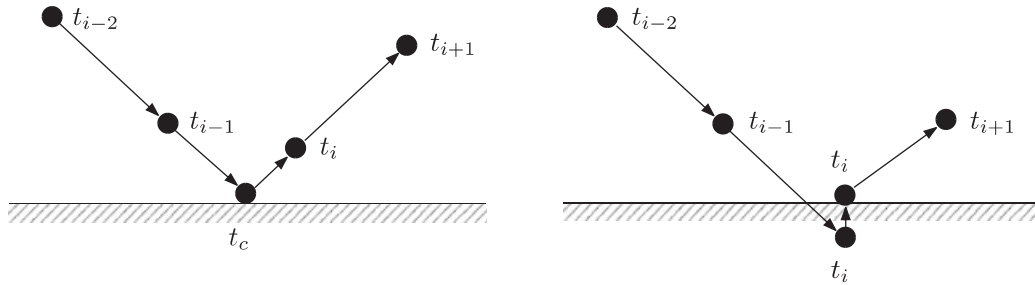


Figure 1. Resolving the impact-time exactly (left) and the approximation used in this paper (right).

To illustrate this, consider a three-dimensional finite element computation with a characteristic element size h . The time-step is thus also of order $\mathcal{O}(h)$, while the number of elements N is proportional to $1/h^3$, so that the total computational cost C will scale like

$$C \propto \frac{N}{\Delta t} \propto 1/h^4 \tag{12}$$

Contact can only occur between the elements on the surface of the solid bodies, so that the number of surface elements involved in impacts is proportional to $1/h^2$. To actually resolve each impact requires time-stepping the entire system exactly to the time of each of the collisions. This implies that the time-step must scale at best like $\mathcal{O}(h^2)$,[§] and so the total work will scale like

$$C \propto \frac{N}{\Delta t} \propto 1/h^5 \tag{13}$$

Clearly this is not feasible, leading to the conclusion that contact simulation algorithms cannot attempt to exactly compute the sequence and timing of all impacts.

In the DCR approach, we do not intend to exactly track the motion of each node through collision and to independently consider each impact. Instead, the equations of motion are initially advanced in time for a time-step $[t_{i-1}, t_i]$ without considering the contact constraints (Figure 1). Subsequently, all the impact events at the time t_i are identified with an algorithm for finding triangle–triangle intersections. For solving the impact equations we make the assumption that the impact event happened at the time t_i . Under these assumptions the impact equations (11) lead to the following quadratic equation system for computing the post-impact velocities:

$$(\lambda \nabla g + \mathbf{p}_{t_i^-})^T \mathbf{M}^{-1} (\lambda \nabla g + \mathbf{p}_{t_i^-}) - \mathbf{p}_{t_i^-}^T \mathbf{M}^{-1} \mathbf{p}_{t_i^-} = 0 \tag{14}$$

The quadratic equation may be solved with iterative methods, such as those of Newton–Raphson type [18]. However, it is also possible to derive closed-form expressions for the post-impact velocities using momentum decompositions as derived in Section 4.

[§]This estimate assumes that no higher frequencies are activated by the refinement. In practice, however, they will be, and so the actual time-step must go to zero faster than $\mathcal{O}(h^2)$, making the cost even higher than that given by (13).

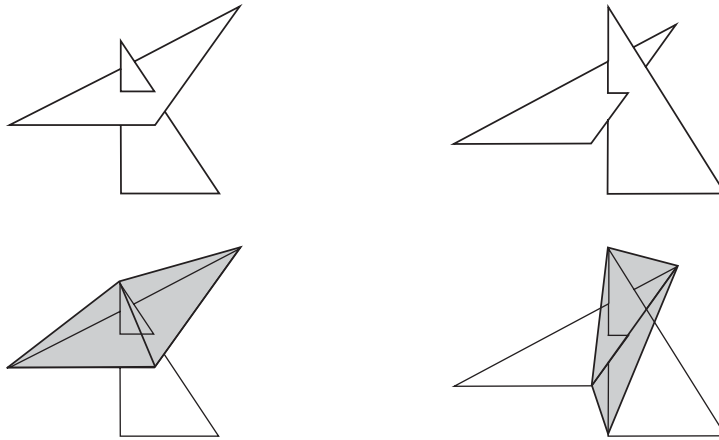


Figure 2. Possible contact surface triangle penetrations and constraint function definitions in three dimensions.

The definition of the constraint function g substantially influences the form and size of the quadratic system of Equation (14). Although it is possible to define the constraints in terms of global geometric quantities, such as intersection volumes, it is advantageous to define the constraints using local quantities only. For three-dimensional problems, essentially two different type impacts are possible: either a node impacts with a finite element face, or the edge of a finite element face impacts with the edge of another face. The two possible types of impacts in three dimensions for triangular finite elements are illustrated in Figure 2. In both cases we can define the constraint function by the signed volume of the tetrahedron formed by one triangle and a vertex, or by two edges, respectively.

The impact equations only describe the changes in the momenta and velocities during the impact event. The enforcement of the constraints on the displacements has to be accomplished independently, e.g. by means of closest point projections. In our implementation in the node–triangle penetration case the penetrating vertex is simply projected back to the closest point on the triangle surface. Similarly, in the edge–edge impact case the penetrating edge is projected to the closest point on the triangle edge. The projecting-back operation of the edges and nodes obviously leads to an increase in the internal energy, which can be taken into account by including the performed work into the energy balance. In the finite element context, the performed work can be readily estimated by multiplying the nodal force vector with the displacement difference to obtain

$$(\lambda \nabla g + \mathbf{p}_{i_i^-})^T \mathbf{M}^{-1} (\lambda \nabla g + \mathbf{p}_{i_i^-}) - \mathbf{p}_{i_i^-}^T \mathbf{M}^{-1} \mathbf{p}_{i_i^-} \approx (\mathbf{f}^{\text{int}} - \mathbf{f}^{\text{ext}}) \cdot (\mathbf{x}_{i_i} - \tilde{\mathbf{x}}_{i_i}) \quad (15)$$

where $\tilde{\mathbf{x}}_{i_i}$ are the projected vertex positions and \mathbf{f}^{int} is the internal force vector. A similar correction can be made to correct the small errors in angular momentum introduced by the projecting-back operation, if desired. In summary, the outline of the overall algorithm for each time-step is given in Figure 3.

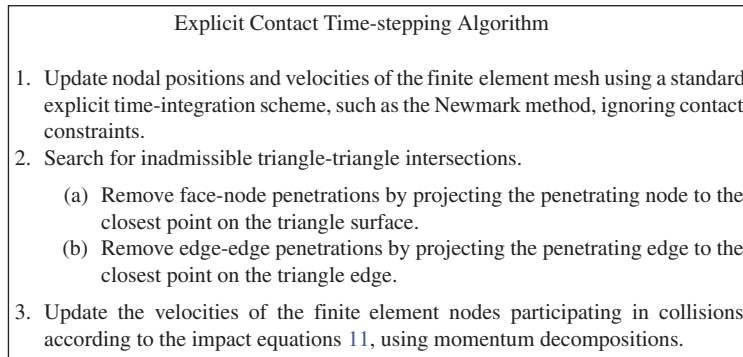


Figure 3. Algorithm for combining time-stepping with explicit contact dynamics. Note that the contact resolution only occurs once per time-step, even though there may be many collisions which occurred within that time. This means that the cost of the time-step scales with element size h as usual for explicit elastodynamics methods, and does not increase faster.

4. MOMENTUM AND VELOCITY DECOMPOSITIONS

A particularly simple method for solving the impact equations (11) can be derived using orthogonal momentum or velocity decompositions. In this section we give a brief outline of the method, which should be sufficient for implementation. In Section 7, we will derive the decompositions in detail and prove the various properties that we use here.

4.1. Non-frictional contact

To begin, the momentum vector of all vertices involved in the impact is decomposed into a normal and a tangential component to give

$$\mathbf{p} = \mathbf{p}_{\text{norm}} + \mathbf{p}_{\text{tang}} \tag{16}$$

The normal component \mathbf{p}_{norm} is defined as the orthogonal projection of the momentum vector onto the span of the gradient of the constraint function, which is

$$\langle \nabla g, \mathbf{p} - \mathbf{p}_{\text{norm}} \rangle_{\mathbf{M}^{-1}} = 0 \tag{17}$$

where $\langle \mathbf{p}, \mathbf{r} \rangle_{\mathbf{M}^{-1}} = \mathbf{p}^T \mathbf{M}^{-1} \mathbf{r}$ is the inner product. Here \mathbf{M} is the mass matrix, and \mathbf{M}^{-1} is its inverse.[¶] The normal component follows from (17) as

$$\begin{aligned} \mathbf{p}_{\text{norm}} &= \left(\frac{\langle \nabla g, \mathbf{p} \rangle_{\mathbf{M}^{-1}}}{\langle \nabla g, \nabla g \rangle_{\mathbf{M}^{-1}}} \right) \nabla g \\ &= (\nabla g)^T \mathbf{M}^{-1} \mathbf{p} [(\nabla g)^T \mathbf{M}^{-1} (\nabla g)]^{-1} \nabla g \end{aligned} \tag{18}$$

[¶]The inner products defined by \mathbf{M} and \mathbf{M}^{-1} are natural for velocities and momenta, respectively. In particular, if $\mathbf{p}_1 = \mathbf{M} \dot{\mathbf{x}}_1$ and $\mathbf{p}_2 = \mathbf{M} \dot{\mathbf{x}}_2$, then $\langle \dot{\mathbf{x}}_1, \dot{\mathbf{x}}_2 \rangle_{\mathbf{M}} = \langle \mathbf{p}_1, \mathbf{p}_2 \rangle_{\mathbf{M}^{-1}}$.

At impact, we write $\mathbf{p}^+ = \mathbf{p}_{t_c}^+$ for the momentum vector immediately after impact, and $\mathbf{p}^- = \mathbf{p}_{t_c}^-$ for momentum vector immediately before impact. These values can be decomposed as above to give

$$\mathbf{p}^+ = \mathbf{p}_{\text{tang}}^+ + \mathbf{p}_{\text{norm}}^+ \quad (19a)$$

$$\mathbf{p}^- = \mathbf{p}_{\text{tang}}^- + \mathbf{p}_{\text{norm}}^- \quad (19b)$$

From (11a) we see that the momentum during the impact jumps by an amount in the direction ∇g . This implies that the tangential components of \mathbf{p} remain the same during impact. Indeed, only the normal component will change. Furthermore, if we take

$$\mathbf{p}_{\text{tang}}^+ = \mathbf{p}_{\text{tang}}^- \quad (20a)$$

$$\mathbf{p}_{\text{norm}}^+ = -\mathbf{p}_{\text{norm}}^- \quad (20b)$$

then we can readily check that energy conservation (11b) is satisfied by computing

$$(\mathbf{p}_{\text{norm}}^+ + \mathbf{p}_{\text{tang}}^+)^T \mathbf{M}^{-1} (\mathbf{p}_{\text{norm}}^+ + \mathbf{p}_{\text{tang}}^+) = (\mathbf{p}^-)^T \mathbf{M}^{-1} (\mathbf{p}^-) \quad (21)$$

where the critical fact is that $\mathbf{p}_{\text{tang}}^-$ and $\mathbf{p}_{\text{norm}}^-$ are orthogonal in the \mathbf{M}^{-1} inner product, so that $(\mathbf{p}_{\text{norm}}^-)^T \mathbf{M}^{-1} (\mathbf{p}_{\text{tang}}^-) = 0$.^{||} Given decomposition (19) of the momentum just before impact into normal and tangential components, we thus see that the momentum just after impact is given by

$$\mathbf{p}^+ = \mathbf{p}_{\text{tang}}^- - \mathbf{p}_{\text{norm}}^- \quad (22)$$

4.2. Inelastic contact

The above impact response based on reversing the normal component of momentum produces entirely elastic impacts. Often it is desirable, however, to include a model of inelastic processes which occur at the instant of impact [19]. The simplest of such models is to take a *coefficient of restitution* $e \in [0, 1]$, which ranges between $e = 1$ for completely elastic to $e = 0$ for completely inelastic contact. The normal component of momentum after impact is now given by

$$\mathbf{p}_{\text{norm}}^+ = -e \mathbf{p}_{\text{norm}}^- \quad (23)$$

An alternative way to express this is to rewrite the impact response (22) as

$$\mathbf{p}^+ = \mathbf{p}^- + \mathbf{I}_{\text{norm}} \quad (24)$$

where the normal impulse is

$$\mathbf{I}_{\text{norm}} = -(1 + e) \mathbf{p}_{\text{norm}}^- \quad (25)$$

^{||}In fact, (20) is the only solution of (11). This can be seen by using (11a) to show that $\mathbf{p}_{\text{norm}}^+$ must be of the form $\mathbf{p}_{\text{norm}}^+ = \alpha \mathbf{p}_{\text{norm}}^-$, assuming non-zero normal component, and then using (11b) to see that $\alpha = 1$ and -1 are the only solutions. The $\alpha = 1$ case corresponds to no impact, and so is ruled out on non-interpenetration grounds, leaving $\alpha = -1$ and giving (20b).

4.3. Sliding directions for friction

We have assumed above that the tangential component of the motion is unchanged by the collision, corresponding to a frictionless impact. To include a model of frictional processes, it is necessary to consider the relative motion between the contacting bodies. As a first step, the momentum is decomposed into non-fixed and fixed components

$$\mathbf{p} = \mathbf{p}_{\text{nonfix}} + \mathbf{p}_{\text{fix}} \tag{26}$$

As the name suggests, the fixed component does not lead to any relative motion between the contacting bodies. For example, the fixed component includes the rigid body translations and rotations of the total system, in addition to other components. In contrast, the non-fixed component may lead to relative motion normal or tangential to the contact surface. For computing the non-fixed components a separation vector \mathbf{h} is defined by

$$\mathbf{h} = \mathbf{x}^L - \mathbf{x}^R \tag{27}$$

where \mathbf{x}^L and \mathbf{x}^R are the positions of the two impacting points, with $\mathbf{h} = \mathbf{0}$ at the impact time t_c .

According to our definition, the fixed component of momentum is such that the fixed velocity $\mathbf{M}^{-1}\mathbf{p}_{\text{fix}}$ instantaneously keeps \mathbf{h} equal to $\mathbf{0}$ (that is, the bodies do not separate, interpenetrate, or slide along each other), so that

$$\mathbf{h}(t_c + \varepsilon) = \nabla\mathbf{h}\mathbf{M}^{-1} \cdot \mathbf{p}_{\text{fix}}\varepsilon + O(\varepsilon^2) = \mathbf{0} \tag{28}$$

which implies

$$\nabla\mathbf{h}\mathbf{M}^{-1} \cdot \mathbf{p}_{\text{fix}} = \mathbf{0} \tag{29}$$

and for the non-fixed components

$$\nabla\mathbf{h}\mathbf{M}^{-1} \cdot (\mathbf{p} - \mathbf{p}_{\text{nonfix}}) = \mathbf{0} \tag{30}$$

Similar to the normal decomposition, the non-fixed component may be interpreted as an orthogonal projection onto the span of the columns of $(\nabla\mathbf{h})^T$ with respect to the inner product \mathbf{M}^{-1} (see Section 7.2 for details). This implies

$$\begin{aligned} \mathbf{p}_{\text{nonfix}} &= (\nabla\mathbf{h})^T \left(\langle (\nabla\mathbf{h})^T, (\nabla\mathbf{h})^T \rangle_{\mathbf{M}^{-1}} \right)^{-1} \langle (\nabla\mathbf{h})^T, \mathbf{p} \rangle_{\mathbf{M}^{-1}} \\ &= (\nabla\mathbf{h})^T [(\nabla\mathbf{h})\mathbf{M}^{-1}(\nabla\mathbf{h})^T]^{-1} (\nabla\mathbf{h})\mathbf{M}^{-1}\mathbf{p} \end{aligned} \tag{31}$$

Non-fixed motions can now be decomposed further into those normal to the impact, leading to separation or interpenetration, and those resulting from sliding between the bodies. We thus have

$$\mathbf{p} = \overbrace{\mathbf{p}_{\text{norm}} + \mathbf{p}_{\text{slide}} + \mathbf{p}_{\text{fix}}}^{\mathbf{p}_{\text{nonfix}}} \tag{32}$$

\mathbf{p}_{tang}

so that the sliding and fixed components are given by

$$\mathbf{p}_{\text{slide}} = \mathbf{p}_{\text{nonfix}} - \mathbf{p}_{\text{norm}} \quad (33)$$

$$\mathbf{p}_{\text{fix}} = \mathbf{p} - \mathbf{p}_{\text{nonfix}} \quad (34)$$

4.4. Frictional impact response

The impact equations (11) assume that the impact occurs without friction. Friction is included by modifying the length of the sliding component of momentum $\mathbf{p}_{\text{slide}}$, as frictional forces are only activated in the direction of potential slippage. As a consequence, frictional forces do not change the total angular and linear momentum of the system (see also Section 7.7).**

We consider here a simple Coulomb model which captures slip–stick behaviour and linear dependence of the frictional force on the normal force.^{††} Friction at the instant of impact is modelled as an impulse, so that the momentum jump equation (11a) becomes

$$\mathbf{p}^+ = \mathbf{p}^- + \mathbf{I}_{\text{norm}} + \mathbf{I}_{\text{slide}} \quad (35)$$

where $\mathbf{I}_{\text{slide}}$ is the impulse in the sliding direction due to friction. For the purposes of computing frictional impulses, we ignore the inelastic model of Section 4.2 and take

$$\mathbf{I}_{\text{norm}} = -2\mathbf{p}_{\text{norm}}^- \quad (36)$$

The corresponding impulse delivered at the point of contact (in \mathbb{R}^3) can be computed from the nodal values by

$$\mathbf{I}_{\text{norm, point}} = (\nabla \mathbf{h})^{-\text{T}} \mathbf{I}_{\text{norm}} \quad (37)$$

with the pseudo-inverse $(\nabla \mathbf{h})^{-1} = (\nabla \mathbf{h})^{\text{T}} (\nabla \mathbf{h} (\nabla \mathbf{h})^{\text{T}})^{-1}$.^{‡‡}

For the subsequent computations we make the assumption that the impulse is delivered over one time-step Δt , so that the normal force component $f_{\text{norm}} \in \mathbb{R}$ at the point of contact is

$$f_{\text{norm}} = \frac{\|\mathbf{I}_{\text{norm, point}}\|}{\Delta t} \quad (38)$$

where $\|\cdot\|$ is the Euclidean norm in \mathbb{R}^3 . In the above and following equations the time-step is used only to clarify the derivation, and does not influence the final result.

The maximum frictional impulse which can be exerted occurs in the case of perfect stick, when the sliding momentum after impact must be $\mathbf{p}_{\text{slide}}^+ = \mathbf{0}$, and so the impulse applied to the system would have to be

$$\mathbf{I}_{\text{slide}}^{\text{max}} = -\mathbf{p}_{\text{slide}}^- \quad (39)$$

**Of course, the angular and linear momenta of the individual bodies involved in the impact will change, but the momenta of the entire system do not.

††More complex models of friction can be easily incorporated into the DCR framework by redefining (45).

‡‡This is well-defined because \mathbf{I}_{norm} is in the direction ∇g , which is in the span of the columns of $(\nabla \mathbf{h})^{\text{T}}$.

Under stick conditions, the impulse $\mathbf{I}_{\text{slide, point}}^{\text{max}}$ and traction $f_{\text{slide}}^{\text{max}} \in \mathbb{R}$ due to friction are thus

$$\mathbf{I}_{\text{slide, point}}^{\text{max}} = (\nabla \mathbf{h})^{-\text{T}} \cdot \mathbf{I}_{\text{slide}}^{\text{max}} \tag{40}$$

$$f_{\text{slide}}^{\text{max}} = \frac{\|\mathbf{I}_{\text{slide, point}}^{\text{max}}\|}{\Delta t} \tag{41}$$

where we use the fact that $\mathbf{I}_{\text{slide}}$ will be in the span of the columns of $(\nabla \mathbf{h})^{\text{T}}$.

For Coulomb’s law of friction, the actual traction f_{slide} depends on the *coefficient of friction* μ , and is given by

$$f_{\text{slide}} = \min\{f_{\text{slide}}^{\text{max}}, \mu f_{\text{norm}}\} \tag{42}$$

Consequently, the actual frictional impulse $\mathbf{I}_{\text{slide, point}}$ at the point of contact and the actual frictional impulse $\mathbf{I}_{\text{slide}}$ of the nodes participating at contact must be

$$\mathbf{I}_{\text{slide, point}} = \frac{f_{\text{slide}}}{f_{\text{slide}}^{\text{max}}} \mathbf{I}_{\text{slide, point}}^{\text{max}} = f_{\text{slide}} \Delta t \frac{\mathbf{I}_{\text{slide, point}}^{\text{max}}}{\|\mathbf{I}_{\text{slide, point}}^{\text{max}}\|} \tag{43}$$

$$\mathbf{I}_{\text{slide}} = (\nabla \mathbf{h})^{\text{T}} \cdot \mathbf{I}_{\text{slide, point}} \tag{44}$$

The preceding sequence of calculations can be collapsed to give

$$\mathbf{I}_{\text{slide}} = \begin{cases} -\mathbf{p}_{\text{slide}}^-, & \|\mathbf{p}_{\text{slide}}^-\|_{\mathbf{M}^{-1}} \leq \mu \|\mathbf{p}_{\text{norm}}^-\|_{\mathbf{M}^{-1}} \\ -\mu \frac{\|\mathbf{p}_{\text{norm}}^-\|_{\mathbf{M}^{-1}}}{\|\mathbf{p}_{\text{slide}}^-\|_{\mathbf{M}^{-1}}} \mathbf{p}_{\text{slide}}^- & \text{otherwise} \end{cases} \tag{45}$$

where $\|\mathbf{p}\|_{\mathbf{M}^{-1}}$ is the norm induced by the inner product $\langle \mathbf{p}, \mathbf{p} \rangle_{\mathbf{M}^{-1}}$. The first case corresponds to perfect stick and the second case to slip. In accordance with the continuous problem, the computed impulse only depends on the momenta prior to contact and does not directly depend on algorithmic variables, such as the time-step or the amount of interpenetration between the bodies before contact resolution.

The entire sequence of calculations to decompose the momentum and compute the impact response is summarized in Figure 4.

4.5. Velocity decompositions

Using the fact that velocity and momentum are related by $\mathbf{p} = \mathbf{M}\dot{\mathbf{x}}$, all of the momentum decompositions can be written as velocity decompositions. We thus have

$$\dot{\mathbf{x}} = \underbrace{\dot{\mathbf{x}}_{\text{norm}}}_{\dot{\mathbf{x}}_{\text{nonfix}}} + \underbrace{\dot{\mathbf{x}}_{\text{slide}} + \dot{\mathbf{x}}_{\text{fix}}}_{\dot{\mathbf{x}}_{\text{tang}}} \tag{46}$$

Decomposition Contact Response (DCR) Algorithm

Input data: momentum \mathbf{p}^- prior to impact, deformed configuration \mathbf{x} of system at impact (so that $g(\mathbf{x}) = 0$), coefficient of restitution e , and coefficient of friction μ .

1. Decompose \mathbf{p}^- by computing $\mathbf{p}_{\text{norm}}^-$ (18), $\mathbf{p}_{\text{nonfix}}^-$ (31), $\mathbf{p}_{\text{slide}}^-$ (33), and $\mathbf{p}_{\text{fix}}^-$ (34).
2. Compute the normal impulse \mathbf{I}_{norm} (25) and the sliding impulse $\mathbf{I}_{\text{slide}}$ (45).
3. Compute the momentum \mathbf{p}^+ just after impact (35).

Figure 4. DCR algorithm for computing the change in momentum due to a impact.

Given a velocity $\dot{\mathbf{x}}$, its normal component is

$$\begin{aligned} \dot{\mathbf{x}}_{\text{norm}} &= \left(\frac{\langle \nabla g, \dot{\mathbf{x}} \rangle}{\langle \nabla g, \nabla g \rangle_{\mathbf{M}^{-1}}} \right) \mathbf{M}^{-1} \nabla g \\ &= (\nabla g)^\top \dot{\mathbf{x}} [(\nabla g)^\top \mathbf{M}^{-1} (\nabla g)]^{-1} \mathbf{M}^{-1} (\nabla g) \end{aligned} \tag{47}$$

and its non-fixed component is

$$\begin{aligned} \dot{\mathbf{x}}_{\text{nonfix}} &= \mathbf{M}^{-1} (\nabla \mathbf{h})^\top (\langle (\nabla \mathbf{h})^\top, (\nabla \mathbf{h})^\top \rangle_{\mathbf{M}^{-1}})^{-1} \langle (\nabla \mathbf{h})^\top, \dot{\mathbf{x}} \rangle \\ &= \mathbf{M}^{-1} (\nabla \mathbf{h})^\top [(\nabla \mathbf{h}) \mathbf{M}^{-1} (\nabla \mathbf{h})^\top]^{-1} (\nabla \mathbf{h}) \dot{\mathbf{x}} \end{aligned} \tag{48}$$

so that the sliding and fixed components are

$$\dot{\mathbf{x}}_{\text{slide}} = \dot{\mathbf{x}}_{\text{nonfix}} - \dot{\mathbf{x}}_{\text{norm}} \tag{49}$$

$$\dot{\mathbf{x}}_{\text{fix}} = \dot{\mathbf{x}} - \dot{\mathbf{x}}_{\text{nonfix}} \tag{50}$$

Note that each component satisfies $\mathbf{p}_{\text{fix}} = \mathbf{M} \dot{\mathbf{x}}_{\text{fix}}$, etc.

5. ILLUSTRATIVE EXAMPLES

5.1. Two particles in 1D

Consider two point masses in 1D with masses m_A and m_B , positions x_A and x_B , and momenta $p_A = m_A \dot{x}_A$ and $p_B = m_B \dot{x}_B$. Assume that initially $x_A < x_B$, so that the admissible set is defined by $g(x_A, x_B) = x_A - x_B \leq 0$. Taking $\mathbf{x} = [x_A \ x_B]^\top$ and $\mathbf{p} = [p_A \ p_B]^\top$ and

$$\mathbf{M} = \begin{bmatrix} m_A & 0 \\ 0 & m_B \end{bmatrix} \tag{51}$$

we have

$$\nabla g(\mathbf{x}) = \begin{bmatrix} 1 \\ -1 \end{bmatrix} \tag{52}$$

The separation vector is given by $h(\mathbf{x}) = x_A - x_B$ and so $\nabla h = \nabla g$. We can now calculate

$$\mathbf{p}_{\text{norm}} = \begin{bmatrix} \frac{m_B p_A - m_A p_B}{m_A + m_B} \\ \frac{m_A p_B - m_B p_A}{m_A + m_B} \end{bmatrix}, \quad \mathbf{p}_{\text{slide}} = \begin{bmatrix} 0 \\ 0 \end{bmatrix}, \quad \mathbf{p}_{\text{fix}} = \begin{bmatrix} \frac{m_A p_A + m_A p_B}{m_A + m_B} \\ \frac{m_B p_A + m_B p_B}{m_A + m_B} \end{bmatrix} \tag{53}$$

It is simple to check that \mathbf{p}_{norm} , $\mathbf{p}_{\text{slide}}$ and \mathbf{p}_{fix} are indeed orthogonal to each other with respect to the inner product $\langle \cdot, \cdot \rangle_{\mathbf{M}^{-1}}$. In particular, $(\mathbf{p}_{\text{norm}})^T \mathbf{M}^{-1} (\mathbf{p}_{\text{fix}}) = 0$, since $\mathbf{p}_{\text{slide}}$ vanishes in the one-dimensional setting. The momentum after a frictionless impact (22) is thus given by $\mathbf{p}^+ = -\mathbf{p}_{\text{norm}}^- + \mathbf{p}_{\text{slide}}^- + \mathbf{p}_{\text{fix}}^-$ which is

$$\mathbf{p}^+ = \frac{1}{m_A + m_B} \begin{bmatrix} m_A - m_B & 2m_A \\ 2m_B & m_B - m_A \end{bmatrix} \begin{bmatrix} p_A \\ p_B \end{bmatrix} \tag{54}$$

and agrees with the familiar formula for an elastic two-particle collision, derived directly from conservation of total linear momentum and total kinetic energy in 1D.

5.2. Node-face impact in 2D

We consider now two linear triangular elements impacting in 2D. As it is the boundaries of the two triangles which actually impact, we need to consider the impact between a point mass and a rigid extensible bar in 2D, as illustrated in Figure 5.

The rod has endpoints \mathbf{x}_A and \mathbf{x}_B , and the point mass has position \mathbf{x}_C . We assume that the mass of the triangles is lumped at the nodes, resulting in masses m_A , m_B , and m_C , with corresponding momenta \mathbf{p}_A , \mathbf{p}_B , and \mathbf{p}_C . We define the constraint function to be

$$g(\mathbf{x}_A, \mathbf{x}_B, \mathbf{x}_C) = (\mathbf{x}_C - \mathbf{x}_B)^T (\mathbf{x}_B - \mathbf{x}_A)^\perp \tag{55}$$

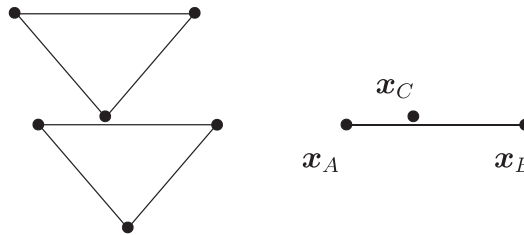


Figure 5. Impact of two triangles in 2D.

where

$$\mathbf{x}^\perp = \begin{bmatrix} x^1 \\ x^2 \end{bmatrix}^\perp = \begin{bmatrix} -x^2 \\ x^1 \end{bmatrix} \tag{56}$$

Note that this is equivalent to taking g to be the third component of the cross product of $(\mathbf{x}_C - \mathbf{x}_B)$ and $(\mathbf{x}_B - \mathbf{x}_A)$ embedded into \mathbb{R}^3 . The function g is thus equal to twice the signed area of the triangle formed by the points \mathbf{x}_A , \mathbf{x}_B and \mathbf{x}_C . Differentiating g with respect to its three arguments gives

$$\nabla_{\mathbf{x}_A} g = (\mathbf{x}_B - \mathbf{x}_C)^\perp, \quad \nabla_{\mathbf{x}_B} g = (\mathbf{x}_C - \mathbf{x}_A)^\perp, \quad \nabla_{\mathbf{x}_C} g = (\mathbf{x}_A - \mathbf{x}_B)^\perp \tag{57}$$

which allows us to compute the normal component of \mathbf{p} using (18).

To form the separation function \mathbf{h} we compute the parameter $\xi \in \mathbb{R}$ such that the impact occurs at $(1 - \xi)\mathbf{x}_A + \xi\mathbf{x}_B$. As this must equal \mathbf{x}_C we have

$$\xi(\mathbf{x}) = \frac{(\mathbf{x}_C - \mathbf{x}_A)^\top (\mathbf{x}_B - \mathbf{x}_A)}{(\mathbf{x}_B - \mathbf{x}_A)^\top (\mathbf{x}_B - \mathbf{x}_A)} \tag{58}$$

The separation vector $\mathbf{h} \in \mathbb{R}^2$ is thus

$$\mathbf{h}(\mathbf{x}) = (1 - \xi)\mathbf{x}_A + \xi\mathbf{x}_B - \mathbf{x}_C \tag{59}$$

and we can calculate the derivative to obtain

$$\nabla \mathbf{h} = \begin{bmatrix} 1 - \xi & 0 & \xi & 0 & -1 & 0 \\ 0 & 1 - \xi & 0 & \xi & 0 & -1 \end{bmatrix} \tag{60}$$

so the transpose of the pseudo-inverse is

$$(\nabla \mathbf{h})^{-T} = \frac{1}{(1 - \xi)^2 + \xi^2 + 1} \begin{bmatrix} 1 - \xi & 0 & \xi & 0 & -1 & 0 \\ 0 & 1 - \xi & 0 & \xi & 0 & -1 \end{bmatrix} \tag{61}$$

To compute the non-fixed component of momentum we use (31), noting that

$$(\nabla \mathbf{h}) \mathbf{M}^{-1} (\nabla \mathbf{h})^\top = \left(\frac{(1 - \xi)^2}{m_1} + \frac{\xi^2}{m_2} + \frac{1}{m_3} \right) \begin{bmatrix} 1 & 0 \\ 0 & 1 \end{bmatrix} \tag{62}$$

The normal component of momentum will be in the direction of ∇g , and the sliding component will be in the remaining part of the span of the rows of $\nabla \mathbf{h}$.

5.3. Momentum decompositions for finite elements

We work here in \mathbb{R}^3 , and consider 2D finite elements which represent either a shell or the boundary of a solid body. Greek indices α, β denote coordinate directions and take values 1, 2, or 3.

Let $N_k(\xi, \eta)$ be the shape function associated with node k , for $k = 1, \dots, n$, where ξ and η are the parameter coordinates of a material point in the element. The nodal positions are

given by $\mathbf{x}^k \in \mathbb{R}^3$ with coordinates $x^{k\alpha}$, so that the total position vector is $\mathbf{x} = [\mathbf{x}^1 \ \mathbf{x}^2 \ \dots \ \mathbf{x}^n]^T$. Similarly, $\dot{\mathbf{x}}^k \in \mathbb{R}^3$ and $\mathbf{p}_k \in \mathbb{R}^3$ are the velocity and momentum vectors of node k .

The $3n \times 3n$ mass matrix \mathbf{M} has components $M_{k\alpha, \ell\beta}$, with a block structure so that $M_{k\alpha, \ell\beta} = m_{k, \ell} \delta_{\alpha\beta}$ for some $n \times n$ matrix \mathbf{m} , where δ is the Kronecker delta. We thus have that $p_{k\alpha} = \sum_{\ell=1}^n \sum_{\beta=1}^3 M_{k\alpha, \ell\beta} v^{\ell\beta} = \sum_{\ell=1}^n m_{k, \ell} v^{\ell\alpha}$.

Normal component. We assume that we have some function $g(\mathbf{x})$ so that the admissible set A is those configurations \mathbf{x} with $g(\mathbf{x}) \leq 0$, as in (3). Using (18) to compute the normal component of velocity now gives

$$[\mathbf{p}_{\text{norm}}]_{k\alpha} = \left(\frac{\sum_{\ell=1}^n \sum_{\beta=1}^3 \sum_{i=1}^n (\partial g(\mathbf{x}) / \partial x^{\ell\beta}) [\mathbf{m}^{-1}]^{\ell, i} p_{i\beta}}{\sum_{\ell=1}^n \sum_{i=1}^n \sum_{\beta=1}^3 (\partial g(\mathbf{x}) / \partial x^{\ell\beta}) [\mathbf{m}^{-1}]^{\ell, i} (\partial g(\mathbf{x}) / \partial x^{i\beta})} \right) \frac{\partial g(\mathbf{x})}{\partial x^{k\alpha}} \tag{63}$$

Sliding component. To calculate $\mathbf{p}_{\text{slide}}$ we must first calculate $\mathbf{p}_{\text{nonfix}}$ using (31). We begin by constructing the separation vector \mathbf{h} which tracks the material points of impact. Let \mathbf{x}^L and \mathbf{x}^R be the positions in \mathbb{R}^3 of the two material particles which impacted, so that

$$x^{L\alpha} = \sum_{k=1}^n N_k(\zeta^L, \eta^L) x^{k\alpha} \tag{64a}$$

$$x^{R\alpha} = \sum_{k=1}^n N_k(\zeta^R, \eta^R) x^{k\alpha} \tag{64b}$$

for material coordinate (ζ^L, η^L) and (ζ^R, η^R) . Now the separation vector is given by $\mathbf{h} = \mathbf{x}^L - \mathbf{x}^R$, as in (27), so $\nabla \mathbf{h}$ is

$$[\nabla \mathbf{h}]_{\ell\beta}^\alpha = \frac{\partial h^\alpha}{\partial x^{\ell\beta}} = (N_\ell(\zeta^L, \eta^L) - N_\ell(\zeta^R, \eta^R)) \delta^\alpha_\beta \tag{65}$$

Using this we can explicitly compute the expression for (31) to give

$$[\mathbf{p}_{\text{nonfix}}]_{k\alpha} = [\Delta N]_k \left(\frac{\sum_{i=1}^n \sum_{j=1}^n [\Delta N]_i [\mathbf{m}^{-1}]^{i, j} p_{j\alpha}}{\sum_{i=1}^n \sum_{j=1}^n [\Delta N]_i [\mathbf{m}^{-1}]^{i, j} [\Delta N]_j} \right) \tag{66}$$

where $[\Delta N]_i = N_i(\zeta^L, \eta^L) - N_i(\zeta^R, \eta^R)$. Note that it is not necessary to calculate the inverse of a matrix in this expression, as the denominator is simply a scalar. This is due to the block structure of \mathbf{M} and $\nabla \mathbf{h}$.

Finally we can obtain $\mathbf{p}_{\text{slide}}$ from

$$[\mathbf{p}_{\text{slide}}]_{k\alpha} = [\mathbf{p}_{\text{nonfix}}]_{k\alpha} - [\mathbf{p}_{\text{norm}}]_{k\alpha} \tag{67}$$

Component properties. In Section 7, we will see that rigid body motions are a subset of the fixed motions, and thus the total linear and angular momentum of the normal and sliding

components is zero, assuming a free system so that g and \mathbf{h} are translation and rotation invariant.^{§§} That is,

$$\mathbf{0} = \sum_{k=1}^n \mathbf{p}_{\text{norm},k} = \sum_{k=1}^n \mathbf{p}_{\text{slide},k} \tag{68a}$$

$$\mathbf{0} = \sum_{k=1}^n (\mathbf{x}^k - \mathbf{x}^{\text{cm}}) \times \mathbf{p}_{\text{norm},k} = \sum_{k=1}^n (\mathbf{x}^k - \mathbf{x}^{\text{cm}}) \times \mathbf{p}_{\text{slide},k} \tag{68b}$$

where the centre of mass \mathbf{x}^{cm} is

$$\mathbf{x}^{\text{cm}} = \frac{\sum_{k=1}^n \sum_{\ell=1}^n m_{k,\ell} \mathbf{x}^k}{\sum_{k=1}^n \sum_{\ell=1}^n m_{k,\ell}} \tag{69}$$

Properties (68) can also be checked by direct calculation.

Lumped mass matrices. For performing the momentum decomposition it is advantageous to use a lumped mass matrix, so that \mathbf{m} is diagonal, making the calculation of \mathbf{m}^{-1} much cheaper. If we assume that \mathbf{m} is diagonal with entries given by m_k , then (63) and (66) simplify to

$$[\mathbf{p}_{\text{norm}}]_{k\alpha} = \left(\frac{\sum_{\ell=1}^n \sum_{\beta=1}^3 (\partial g(\mathbf{x}) / \partial x^{\ell\beta}) (m_\ell)^{-1} p_{\ell\beta}}{\sum_{\ell=1}^n \sum_{\beta=1}^3 (\partial g(\mathbf{x}) / \partial x^{\ell\beta}) (m_\ell)^{-1} (\partial g(\mathbf{x}) / \partial x^{\ell\beta})} \right) \frac{\partial g(\mathbf{x})}{\partial x^{k\alpha}} \tag{70a}$$

$$[\mathbf{p}_{\text{nonfix}}]_{k\alpha} = [\Delta N]_k \left(\frac{\sum_{\ell=1}^n [\Delta N]_\ell (m_\ell)^{-1} p_{\ell\alpha}}{\sum_{\ell=1}^n [\Delta N]_\ell (m_\ell)^{-1} [\Delta N]_\ell} \right) \tag{70b}$$

Even in cases where lumped mass matrices are not being used for the finite element discretization, it may be reasonable to use mass lumping for the contact response step of the DCR algorithm.

6. NUMERICAL EXAMPLES

In this section, we investigate the performance of the proposed DCR algorithm for selected contact problems in one and three-dimensions. All three-dimensional examples are discretized with subdivision shell elements [20–22]. The time-integration is performed with the explicit Newmark scheme without physical or algorithmic damping ($\beta = 0.0, \gamma = 0.5$).

6.1. Two-bar impact

We consider first the longitudinal impact of two identical bars (Figure 6). The length of each bar is $L = 10$, Young’s modulus is $E = 1$, mass density is $\rho = 1$, and the cross-section is

^{§§}This will not be true if there are elements of the system, such as a fixed wall, which do not move if the position vector \mathbf{x} is translated or rotated, and in such cases we do not expect momentum preservation during impact.

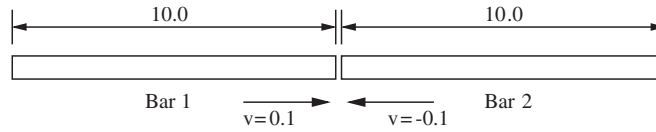


Figure 6. Impact of two bars.

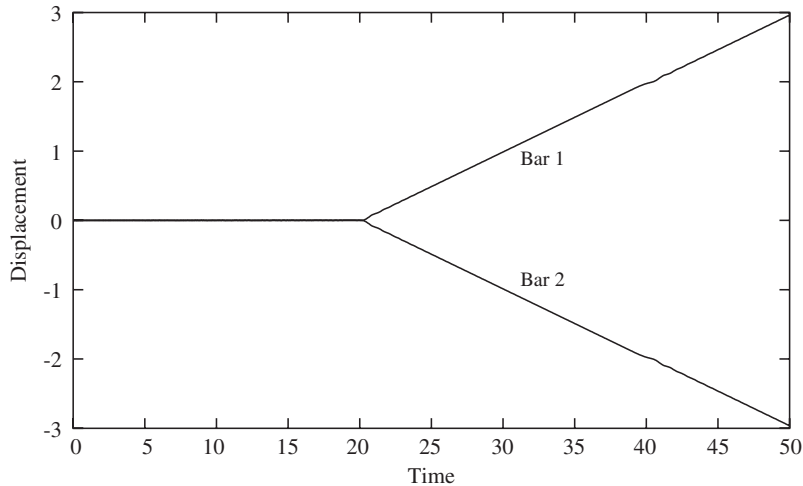


Figure 7. Two-bar impact. Tip displacements versus time.

$A = 1.0$. Prior to impact at $t = 0$, the velocities of the left and right bar are $v = 0.1$ and -0.1 , respectively. In the numerical computations both bars are discretized with 100 two-node linear elastic finite elements. The stable time step size, or the Courant number, is $\Delta t_c = 0.1$. Two different computations with time step sizes $\Delta t = 0.05$ and 0.01 are performed. The displacements of the contacting bar tips is shown in Figure 7 and is essentially independent of the time size. In agreement with the analytical solution, the bar tips remain in contact for $t < 20$. In contrast to the displacements, the velocities exhibit spurious oscillations as shown in Figures 8 and 9. The oscillations can essentially be attributed to the explicit character of the DCR algorithm and the absence of numerical damping. Nevertheless, the oscillations get smaller as the time step size is decreased, particularly during the persistent contact phase ($t < 20$).

6.2. Sphere–sphere impact

As a more complex example, we consider the impact of two shell spheres discretized with 4096 subdivision shell elements, as shown in Figure 10. Both spheres have radius $R = 1.0$ and thickness $h = 0.05$. Young’s modulus is $E = 2.1 \times 10^5$, Poisson’s ratio is $\nu = 0.3$, and the mass density is $\rho = 7.85 \times 10^{-2}$. Prior to the impact the sphere on the left has an initial velocity of $v_x = 150.0$, $v_y = 0.0$, and $v_z = 0.0$ and the sphere on the right has a velocity of $v_x = -50.0$, $v_y = 0.0$, and $v_z = 0.0$. The time-step for the explicit Newmark scheme has been chosen as $\Delta t = 5 \times 10^{-6}$.

As it is visible in the snapshots of Figure 10, the impact process leads to significant deformations of both spheres due to the relatively small radius-to-thickness ratio. Furthermore,

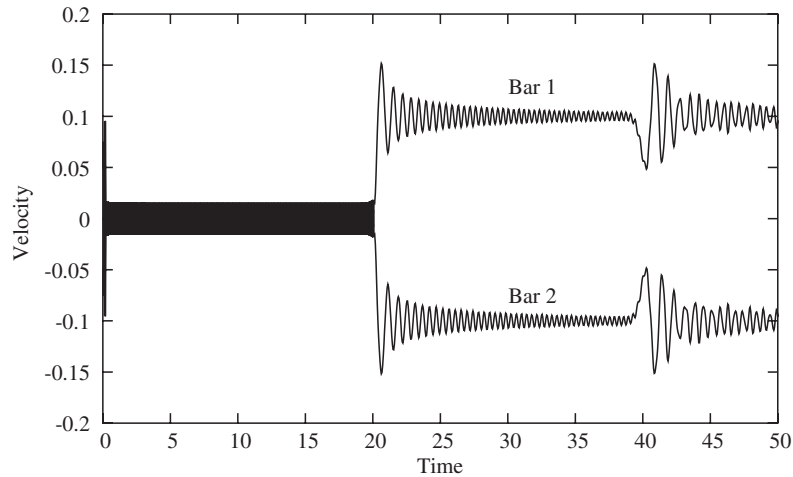


Figure 8. Two-bar impact. Tip velocities versus time for $\Delta t = 0.05$.

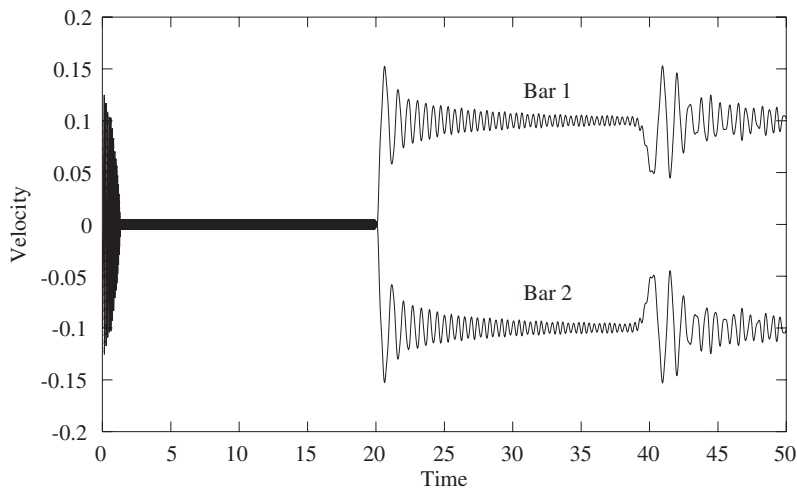


Figure 9. Two-bar impact. Tip velocities versus time for $\Delta t = 0.01$.

during the impact process a significant part of the kinetic energy is converted into internal energy (Figure 11). The slight total energy increase by 2.58% during the impact is caused by the energy contributed to system during the removal of the penetrations. We did not apply the modification proposed in Equation (15), since the energy increase appears to be insignificant. The total angular and linear momentum of the system are practically constant throughout the simulation, as is evident from Figure 12.

In the frictional case, the total energy of the system decays in time as a result of energy dissipation caused by the slip-type frictional response (see Figure 13). In Figure 14, it can be seen that for small amounts of friction ($\mu = 0.25$ and 0.5) slip-type friction dominates and as a result the energy decrease is greater for higher friction. For larger amounts of friction ($\mu = 0.75$

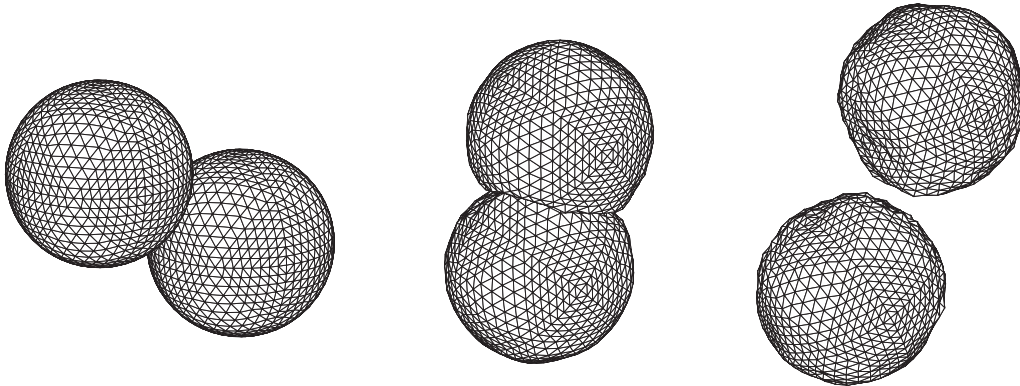


Figure 10. Impact of two spheres at $t = 0, 0.02$ and 0.03 .

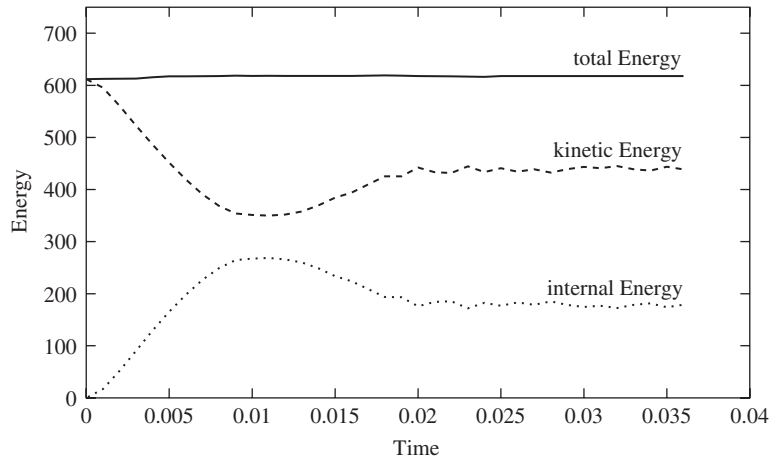


Figure 11. Sphere–sphere impact with $\mu = 0.0$. Energies versus time.

and 1.0), in contrast, stick-type friction becomes increasingly important, so that the energy loss lessens as the friction coefficient rises. The DCR algorithm essentially conserves the momenta independent of the friction parameters, so that the time history of the total momenta with friction is indistinguishable from Figure 12.

6.3. Non-smooth cube impact

Our third example concerns the non-frictional impact of five cubes (Figure 15). The impacts between the non-smooth cubes require the treatment of both vertex–triangle and edge–edge impacts. Each cube has an edge length of 1.0 and has been discretized with 192 subdivision shell elements. Young’s modulus is $E = 2.1 \times 10^5$, Poisson’s ratio is $\nu = 0.3$, and the mass density is $\rho = 0.7085$. Prior to the impact, the single cube has a uniform initial velocity

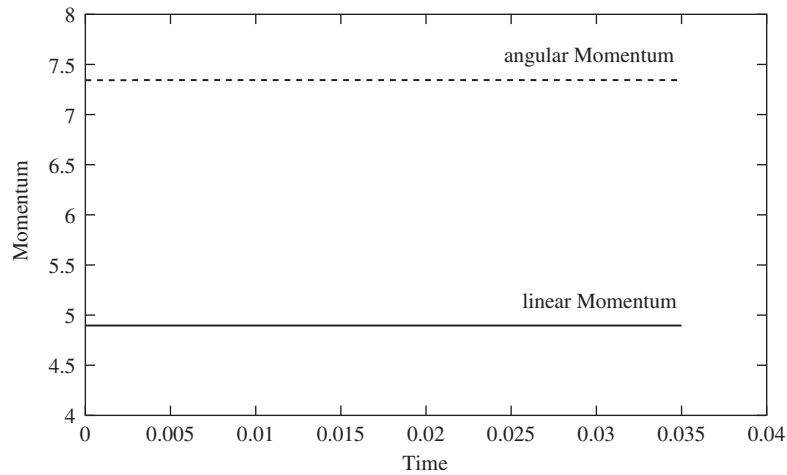


Figure 12. Sphere-sphere impact with $\mu=0.0$. Norm of momenta versus time.

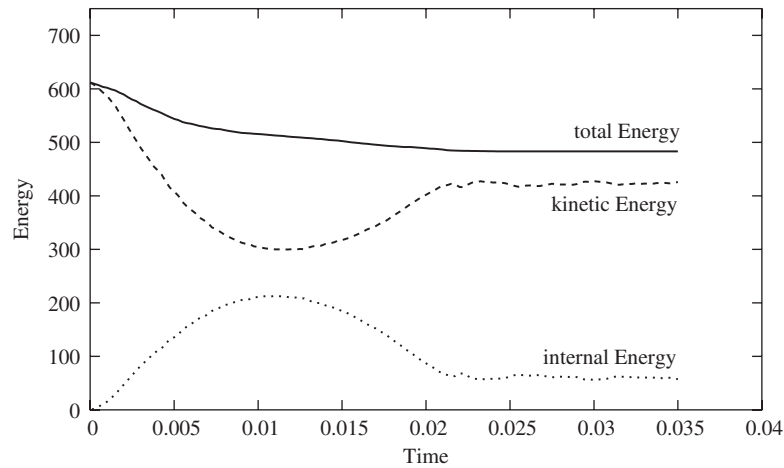


Figure 13. Sphere-sphere impact with $\mu=0.5$. Energies versus time.

of $v_x = 30.0$, $v_y = -30.0$, and $v_z = -30.0$, and the group of four cubes have $v_x = -30.0$, $v_y = 30.0$, and $v_z = 30.0$. The time-step for the explicit Newmark scheme has been chosen as $\Delta t = 5 \times 10^{-6}$. Again, the very good energy and momentum conservation properties of the proposed method are noteworthy (Figures 16 and 17).

Figures 18 and 19 show the collision of 76 cubes discretized with 14592 subdivision shell elements. The geometry of each cube, spatial discretization, and time-integration parameters are equivalent to the five cube case. The robustness of the proposed DCR algorithm is evident in this highly complex problem, which includes both smooth and non-smooth contact.

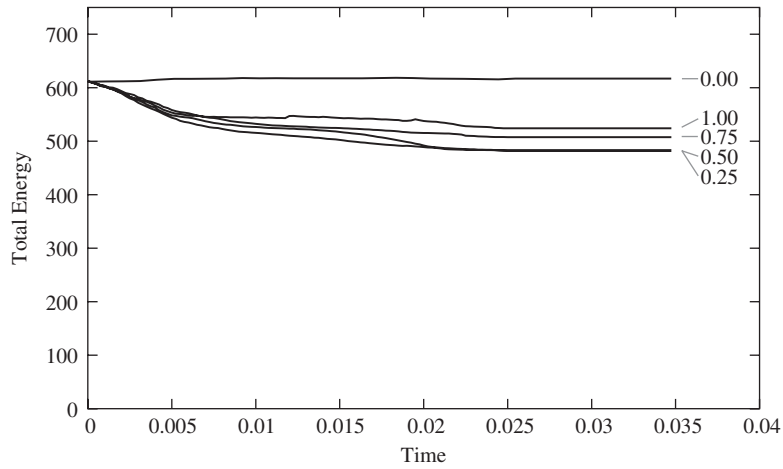


Figure 14. Sphere–sphere impact with $\mu = 0.00, 0.25, 0.50, 0.75,$ and 1.00 . Total energy versus time.

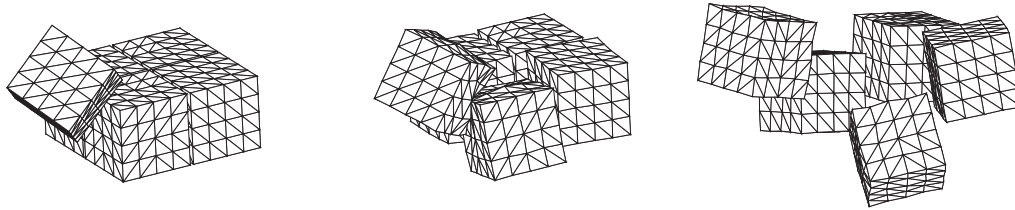


Figure 15. Impact of five cubes at $t = 0, 0.0075,$ and 0.015 .

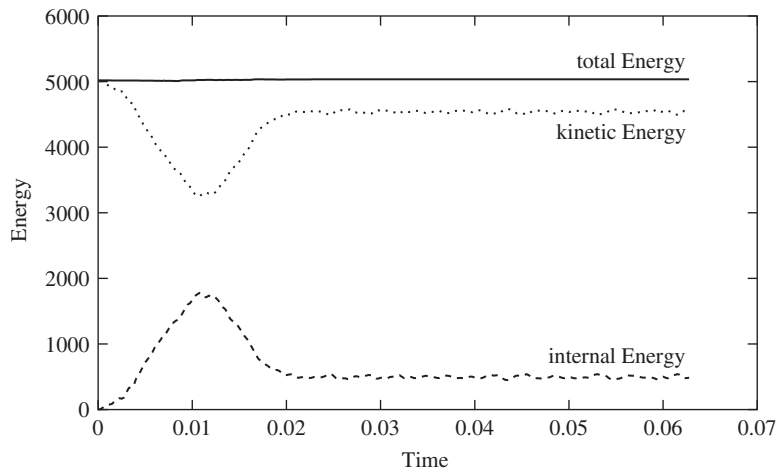


Figure 16. Non-smooth cube impact. Energies versus time.

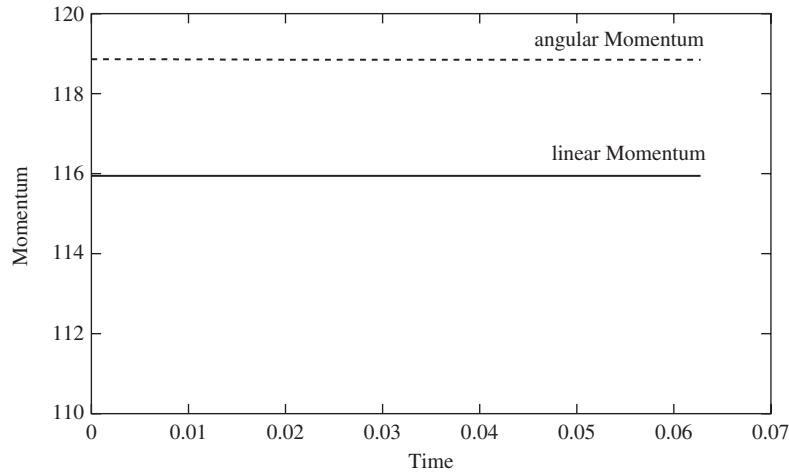


Figure 17. Non-smooth cube impact. Norm of momenta versus time.

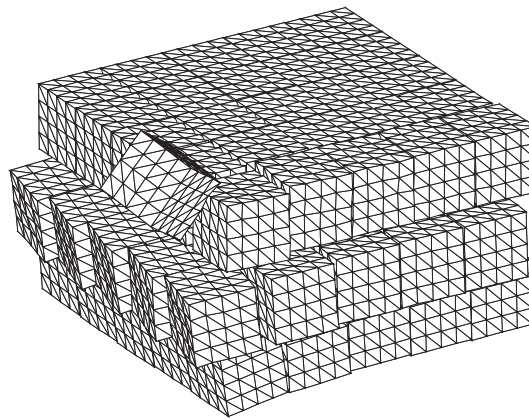


Figure 18. Impact of 76 cubes at $t = 0.028$.

6.4. Sphere–plate impact

Our last example, the impact of a spherical shell with a plate illustrates the performance of the DCR for situations with mainly persistent contact. The sphere and plate have a thickness $h = 0.0035$, and the radii are $R = 0.35$ and 0.125 , respectively. The Young's modulus is $E = 2.1 \times 10^5$, the Poisson's ratio is $\nu = 0.3$, and the mass density is $\rho = 7.85 \times 10^{-2}$. The sphere has an uniform initial velocity of $v_z = -75.0$ and the plate has $v_z = 25.0$. The time-step for the explicit Newmark scheme has been chosen as $\Delta t = 1 \times 10^{-7}$.

The finite element mesh with 6528 subdivision shell elements and two snapshots of the limit surface at $t = 0.0015$ and 0.0030 are shown in Figure 20. The localized strong oscillations in the internal and kinetic energy histories in Figure 21 result from the wave reflection at the free-plate boundary. Furthermore, the weak linear momentum oscillations in Figure 22 result

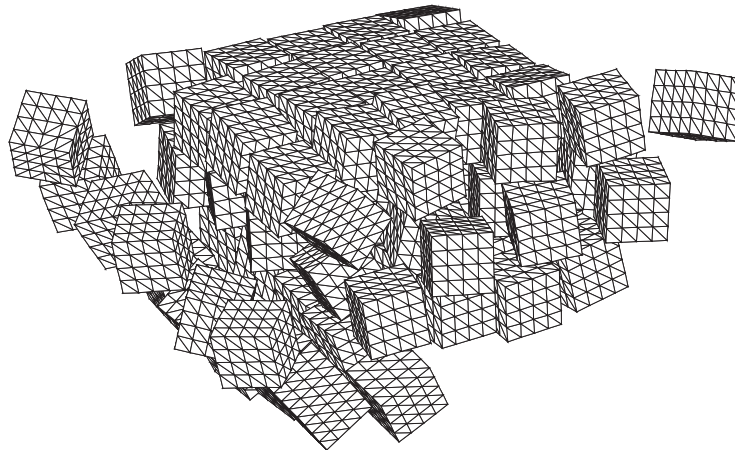


Figure 19. Impact of 76 cubes at $t = 0.21$.

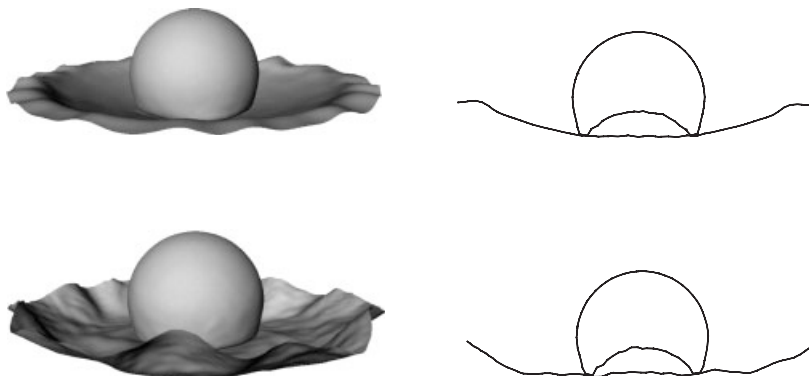
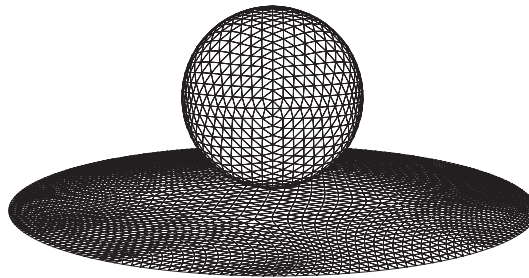


Figure 20. Impact of a sphere and a plate at $t = 0, 0.0015$ and 0.0030 .

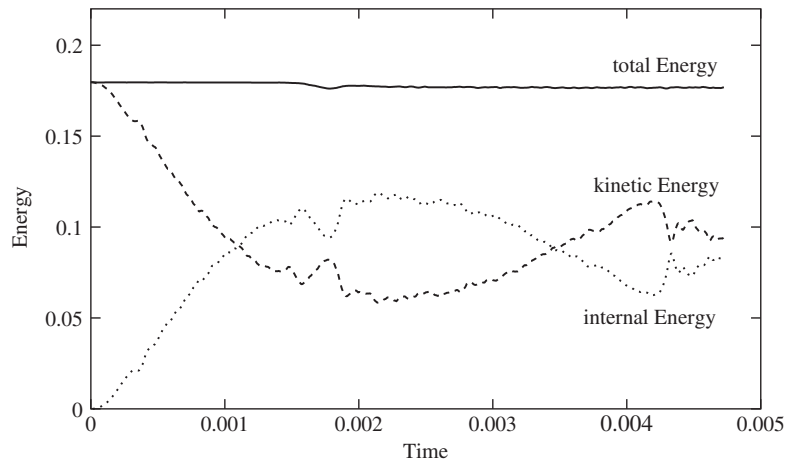


Figure 21. Sphere-plate impact. Energies versus time.

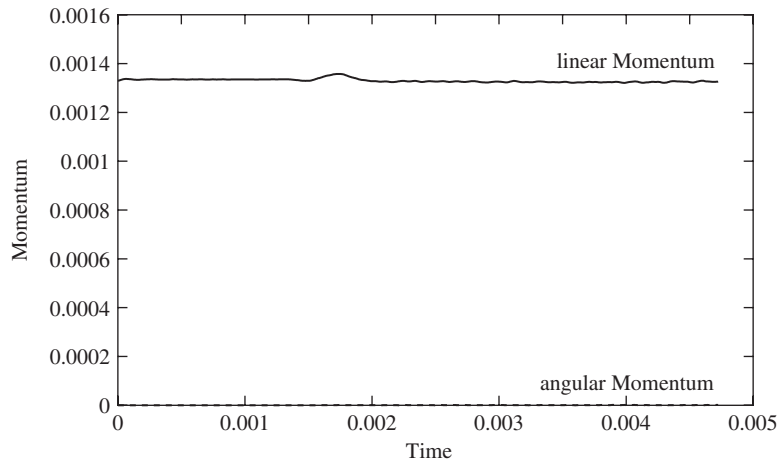


Figure 22. Sphere-plate impact. Norm of momenta versus time.

from the non-conservative dynamic boundary condition enforcement for the subdivision shell elements. Despite the oscillations the good energy and momentum conservation properties of the method are apparent.

7. INTRINSIC MOMENTUM DECOMPOSITIONS

In this section, we revisit the momentum and velocity decompositions of Section 4 from an intrinsic point of view. This allows us to be more precise about the definitions and properties

of the decompositions, as well as readily enabling the definition of a fourth component, namely rigid motions, which makes clear the momentum preserving properties of the DCR method.

7.1. System geometry

The notation used in this section is substantially different from that in Sections 1–6. Here we use standard differential-geometric notation, such as that in Reference [23].

Consider a configuration manifold Q , with the tangent space $T_q Q$ consisting of all velocity vectors based at the configuration $q \in Q$. We take a Riemannian metric on Q , given by

$$\langle v, w \rangle_M = v^T M(q) w \tag{71}$$

for some positive definite matrix $M(q)$ ^{¶¶} and all $v, w \in T_q Q$, with coordinate expression $[M(q)]_{ij}$.

The dual space to $T_q Q$ is the cotangent space $T_q^* Q$, consisting of momentum or force vectors based at the point $q \in Q$. The inner product $M(q)$ on $T_q Q$ induces the Legendre transform $M(q) = \mathbb{F}L|_{T_q Q} : T_q Q \rightarrow T_q^* Q$ by $\langle M(q)v, w \rangle = \langle v, w \rangle_{M(q)}$, with coordinate expression $p_i = [M(q)]_{ij} v^j$. It also induces an inner product $\langle \cdot, \cdot \rangle_{M(q)^{-1}}$ on $T_q^* Q$ by $\langle p, r \rangle_{M(q)^{-1}} = \langle p, M(q)^{-1} r \rangle$ with coordinate expression $[M(q)^{-1}]^{ij}$, where $\langle \cdot, \cdot \rangle$ denotes dual-primal pairing.

Let $A \subset Q$ be the admissible set of configurations, and ∂A be the contact set. We assume that A is defined by

$$A = \{q \in Q \mid g(q) \leq 0\} \tag{72}$$

for some smooth admissible set function $g : Q \rightarrow \mathbb{R}$ for which 0 is a regular value.^{¶¶¶} Henceforth, we will assume that q is a point in ∂A at which we work.

7.2. Projection operators

We briefly recall some elementary facts concerning projection operators. Consider a linear space X with an inner product M , and let $B : X \rightarrow Y$ be a linear operator from X onto Y . Then we have

$$\begin{array}{ccc} (X, M) & \xrightarrow{B} & (Y, N) \\ M \downarrow & & \downarrow N \\ (X^*, M^{-1}) & \xleftarrow{B^*} & (Y^*, N^{-1}) \end{array} \tag{73}$$

where X^* and Y^* are dual spaces, B^* is the adjoint of B , and N is defined by the induced inner product on Y^* given by $\langle r, \bar{r} \rangle_{N^{-1}} = \langle B^* r, B^* \bar{r} \rangle_{M^{-1}}$. As matrices, $[B^*] = [B]^T$ and

^{¶¶}The matrix $M(q)$ corresponds to the (possibly configuration dependent) mass matrix of earlier sections.

^{¶¶¶}That is, if $g(q) = 0$ then $dg(q) \neq 0$.

$N = [BM^{-1}B^T]^{-1}$. Given these constructions, we now observe that

$$X^* = \text{range}(B^*) \oplus (M \cdot \ker(B)) \tag{74a}$$

$$\text{range}(B^*) \perp_{M^{-1}} (M \cdot \ker(B)) \tag{74b}$$

To see (74b) we take $B^*r \in \text{range}(B^*)$ and $p \in M \cdot \ker(B)$, so that $BM^{-1}p = 0$, and calculate $\langle B^*r, p \rangle_{M^{-1}} = \langle r, BM^{-1}p \rangle = 0$. To see (74a) we already have that the intersection of the two spaces is $\{0\}$, and we now write the projection operators explicitly as

$$\mathbb{P}_1 = B^*NBM^{-1} \tag{75a}$$

$$\mathbb{P}_2 = \text{Id} - \mathbb{P}_1 \tag{75b}$$

Clearly $\mathbb{P}_1(p) \in \text{range}(B^*)$, so we only need to check that $\mathbb{P}_2(p) \in M \cdot \ker(B)$, but this follows immediately from

$$BM^{-1}(\text{Id} - B^*NBM^{-1}) = BM^{-1} - (BM^{-1}B^*)(BM^{-1}B^*)^{-1}BM^{-1} = 0$$

7.3. Momentum and velocity decompositions

The tangent and cotangent spaces are decomposed into

$$T_q Q = \underbrace{T_q^{\text{nonfix}} Q}_{T_q^{\text{norm}} Q \oplus T_q^{\text{slide}} Q} \oplus \underbrace{T_q^{\text{fix}} Q}_{T_q^{\text{rigid}} Q \oplus T_q^{\text{shape}} Q} \tag{76a}$$

$T_q^{\text{tang}} Q$

$$T_q^* Q = \underbrace{T_q^{*, \text{nonfix}} Q}_{T_q^{*, \text{norm}} Q \oplus T_q^{*, \text{slide}} Q} \oplus \underbrace{T_q^{*, \text{fix}} Q}_{T_q^{*, \text{rigid}} Q \oplus T_q^{*, \text{shape}} Q} \tag{76b}$$

$T_q^{*, \text{tang}} Q$

where all non-intersecting subspaces are orthogonal in the appropriate inner product (that is, $M(q)$ for $T_q Q$ and $M(q)^{-1}$ for $T_q^* Q$) and the corresponding components of $T_q^* Q$ and $T_q Q$ are images under $M(q)$. The orthogonal projection operators onto the subspaces of the tangent and cotangent spaces are denoted by

$$\mathbb{P}_X : T_q Q \rightarrow T_q^X Q, \quad \mathbb{P}_{*,X} : T_q^* Q \rightarrow T_q^{*,X} Q \tag{77}$$

where X denotes any of the subspaces. Given a velocity $v \in T_q Q$ and corresponding momentum $p = Mv \in T_q^* Q$, these can be decomposed into

$$v = \underbrace{v_{\text{norm}} + v_{\text{slide}}}_{v_{\text{tang}}} + \underbrace{v_{\text{rigid}} + v_{\text{shape}}}_{v_{\text{fix}}} \tag{78a}$$

$$p = \underbrace{p_{\text{norm}} + p_{\text{slide}}}_{p_{\text{tang}}} + \underbrace{p_{\text{rigid}} + p_{\text{shape}}}_{p_{\text{fix}}} \tag{78b}$$

where the various components are the projections with the corresponding operators (77). The components of v and p are thus mutually orthogonal with respect to the appropriate inner products, and are individually related by $M(q)$.

7.4. Normal and tangential components

We define the normal and tangential subspaces to be

$$T_q^{\text{norm}} Q = M(q)^{-1} \cdot T_q^{*, \text{norm}} Q, \quad T_q^{*, \text{norm}} Q = \text{span}\{\text{dg}(q)\} \tag{79a}$$

$$T_q^{\text{tang}} Q = (T_q^{\text{norm}} Q)^\perp, \quad T_q^{*, \text{tang}} Q = (T_q^{*, \text{norm}} Q)^\perp \tag{79b}$$

so that $T_q^{*, \text{tang}} Q = M(q) \cdot T_q^{\text{tang}} Q$. Note also that

$$T_q^{\text{tang}} Q = \ker(\text{dg}(q)) \tag{80}$$

The projections onto the normal subspaces are given explicitly by

$$v_{\text{norm}} = \mathbb{P}_{\text{norm}}(v) = \left(\frac{\langle \text{dg}(q), v \rangle}{\langle \text{dg}(q), \text{dg}(q) \rangle_{M(q)^{-1}}} \right) M(q)^{-1} \text{dg}(q) \tag{81a}$$

$$p_{\text{norm}} = \mathbb{P}_{*, \text{norm}}(p) = \left(\frac{\langle p, \text{dg}(q) \rangle_{M(q)^{-1}}}{\langle \text{dg}(q), \text{dg}(q) \rangle_{M(q)^{-1}}} \right) \text{dg}(q) \tag{81b}$$

7.5. Fixed, non-fixed and sliding components

We assume that our system is modelling a continuum mechanical system in \mathbb{R}^3 and that the impact at $q \in \partial A$ occurs at a spatial location $x \in \mathbb{R}^3$ between two material particles. Let $\langle \cdot, \cdot \rangle_D$ be an inner product on $T_0 \mathbb{R}^3$ with the associated norm $\|\cdot\|_D$, giving the magnitude of velocity vectors. Coordinate indices a, b, c range over 1, 2, 3, so that D has coordinate representation $[D]_{ab}$. The induced inner product on $T_0^* \mathbb{R}^3$ is $\langle \cdot, \cdot \rangle_{D^{-1}}$ with coordinate representation $[D^{-1}]^{ab}$. We define maps

$$h_q^1, h_q^2 : Q \rightarrow \mathbb{R}^3 \tag{82}$$

so that for some other configuration $\tilde{q} \in Q$ the expressions $h_q^1(\tilde{q})$ and $h_q^2(\tilde{q})$ give the positions in \mathbb{R}^3 of the two material particles which impacted at configuration q . By definition we have $h_q^1(q) = h_q^2(q)$. Now define $h_q : Q \rightarrow \mathbb{R}^3$ by

$$h_q(\tilde{q}) = h_q^1(\tilde{q}) - h_q^2(\tilde{q}) \tag{83}$$

so that $h_q(\tilde{q})$ gives the separation in configuration \tilde{q} between the two points which impacted in configuration q . Note that $h_q(q) = 0$. A trajectory $q(t)$ consists of purely fixed motion if $q(t) \in \partial A$, so that $h_{q(0)}(q(t)) = 0$ for some $q(0) \in \partial A$ and all times t .

The infinitesimal version of this means that a velocity $v \in T_q Q$ is a purely fixed direction if $T_q h_q(v) = 0$, where $T_q h_q : T_q Q \rightarrow T_0 \mathbb{R}^3$ is the tangent map of h at q , with corresponding adjoint map $T_q^* h_q : T_0^* \mathbb{R}^3 \rightarrow T_q^* Q$. We thus define

$$T_q^{\text{fix}} Q = \ker(T_q h_q) \tag{84}$$

and using (75) the non-fixed, fixed and sliding subspaces are thus

$$T_q^{\text{nonfix}} Q = M(q)^{-1} \cdot T_q^{*, \text{nonfix}} Q, \quad T_q^{*, \text{nonfix}} Q = \text{range}(T_q^* h_q) \tag{85a}$$

$$T_q^{\text{fix}} Q = (T_q^{\text{nonfix}} Q)^\perp, \quad T_q^{*, \text{fix}} Q = (T_q^{*, \text{nonfix}} Q)^\perp \tag{85b}$$

$$T_q^{\text{slide}} Q = T_q^{\text{nonfix}} Q \cap T_q^{\text{tang}} Q, \quad T_q^{*, \text{slide}} Q = T_q^{*, \text{nonfix}} Q \cap T_q^{*, \text{tang}} Q \tag{85c}$$

so that $T_q^{*, \text{fix}} Q = M(q) \cdot T_q^{\text{fix}} Q$ and $T_q^{*, \text{slide}} Q = M(q) \cdot T_q^{\text{slide}} Q$.

For h_q to be a well-defined separation map, it must be compatible with the admissible set map g in the sense that if $g(q) = 0$ and $h_q(\tilde{q}) = 0$ then $g(\tilde{q}) = 0$. This implies that $h_q^{-1}(0) \subset g^{-1}(0)$ and so $dg(q) \in \text{range}(T_q^* h_q)$. From (79a) and (85a), this is simply the statement that $T_q^{*, \text{norm}} Q \subset T_q^{*, \text{nonfix}} Q$, as required.

Following Section 7.2, the adjoint map $T_q^* h_q$ can also be used to induce an inner product $\langle \cdot, \cdot \rangle_{C(q)^{-1}}$ on $T_0^* \mathbb{R}^3$ by $\langle u, w \rangle_{C(q)^{-1}} = \langle T_q^* h_q u, T_q^* h_q w \rangle_{M(q)^{-1}}$, with the corresponding map $C(q) : T_0 \mathbb{R}^3 \rightarrow T_0^* \mathbb{R}^3$ and the inner product $\langle \cdot, \cdot \rangle_{C(q)}$ on $T_0 \mathbb{R}^3$. Arranged as a commutative diagram this gives

$$\begin{array}{ccc} (T_q Q, M(q)) & \xrightarrow{T_q h_q} & (T_0 \mathbb{R}^3, C(q)) \\ M(q) \downarrow & & C(q) \downarrow \\ (T_q^* Q, M(q)^{-1}) & \xleftarrow{T_q^* h_q} & (T_0^* \mathbb{R}^3, C(q)^{-1}) \end{array} \tag{86}$$

We assume that there is a scalar function $\beta : Q \rightarrow \mathbb{R}$ such that the natural inner product D and the induced inner product $C(q)$ on $T_0 \mathbb{R}^3$ are related by $\langle u, w \rangle_{C(q)} = \beta(q) \langle u, w \rangle_D$ (all standard continuum mechanics examples satisfy this assumption).

We can thus decompose $T_0 \mathbb{R}^3$ and $T_0^* \mathbb{R}^3$ into

$$T_0 \mathbb{R}^3 = T_0^{\text{norm}} \mathbb{R}^3 \oplus T_0^{\text{slide}} \mathbb{R}^3 \tag{87a}$$

$$T_0^* \mathbb{R}^3 = T_0^{*, \text{norm}} \mathbb{R}^3 \oplus T_0^{*, \text{slide}} \mathbb{R}^3 \tag{87b}$$

where the spaces are defined by

$$T_0^{\text{norm}} \mathbb{R}^3 = T_q h_q \cdot T_q^{\text{norm}} Q, \quad T_0^{\text{slide}} \mathbb{R}^3 = T_q h_q \cdot T_q^{\text{slide}} Q \tag{88a}$$

$$T_0^{*, \text{norm}} \mathbb{R}^3 = (T_q^* h_q)^{-1} \cdot T_q^{*, \text{norm}} Q, \quad T_0^{*, \text{slide}} \mathbb{R}^3 = (T_q^* h_q)^{-1} \cdot T_q^{*, \text{slide}} Q \tag{88b}$$

so that the normal and sliding subspaces are orthogonal in both the D and $C(q)$ inner products, and the tangent subspaces are the images under D and $C(q)$ of the respective cotangent subspaces. Note that decomposition (87) depends on the reference point $q \in \partial A$ at which we are working.

We have the adjoint map $C(q)^*: T_0^* \mathbb{R}^3 \rightarrow T_0^{**} \mathbb{R}^3 \cong T_0 \mathbb{R}^3$, as $T_0 \mathbb{R}^3$ is finite dimensional and hence reflexive. Using this we can explicitly compute the projection operators (75) to be

$$\mathbb{P}_{\text{nonfix}} = M(q)^{-1} \cdot T_q^* h_q \cdot C(q)^* \cdot T_q h_q \tag{89a}$$

$$\mathbb{P}_{*, \text{nonfix}} = T_q^* h_q \cdot C(q)^* \cdot T_q h_q \cdot M(q)^{-1} \tag{89b}$$

$$\mathbb{P}_{\text{slide}} = \mathbb{P}_{\text{nonfix}} - \mathbb{P}_{\text{norm}} \tag{89c}$$

$$\mathbb{P}_{*, \text{slide}} = \mathbb{P}_{*, \text{nonfix}} - \mathbb{P}_{*, \text{norm}} \tag{89d}$$

which recovers (31) and (48).

7.6. Rigid and shape components

Now let G^{rigid} be a Lie group with Lie algebra $\mathfrak{g}^{\text{rigid}}$ acting on Q , which represents the allowable *rigid-body motions*. Coordinates on $\mathfrak{g}^{\text{rigid}}$ are indexed by α, β . Typically G^{rigid} will be $SE(3)$ or some subset thereof. We assume that G^{rigid} acts freely on Q , and that the admissible set function g is invariant under the action of G^{rigid} , and thus so is the admissible set A itself. In addition, we take the impact point separation function h to be invariant. We denote by $\xi_Q: Q \rightarrow TQ$ the infinitesimal generator corresponding to each element $\xi \in \mathfrak{g}$ of the Lie algebra and define the map $L(q): \mathfrak{g}^{\text{rigid}} \rightarrow T_q Q$ by

$$L(q)(\xi) = \xi_Q(q) \tag{90}$$

which is linear and one-to-one, as the action is free. The coordinate expression for $L(q)$ is given by $[L(q)]_\alpha^i$ and the *adjoint* map $L(q)^*: T_q^* Q \rightarrow (\mathfrak{g}^{\text{rigid}})^*$ defined by $\langle L(q)^* p, \xi \rangle = \langle p, L(q)\xi \rangle$ has coordinate expression $[L(q)^*]_\alpha^i = [L(q)]_\alpha^i$.

As in Section 7.2, the inner product on $T_q Q$ naturally induces an inner product $\langle \cdot, \cdot \rangle_{\mathbb{I}(q)}$ on $\mathfrak{g}^{\text{rigid}}$ by $\langle \xi, \psi \rangle_{\mathbb{I}(q)} = \langle L\xi, L\psi \rangle_{M(q)}$. The operator $\mathbb{I}(q): \mathfrak{g}^{\text{rigid}} \times \mathfrak{g}^{\text{rigid}} \rightarrow \mathbb{R}$ is known as the *locked inertia tensor* and can be expressed as

$$\langle \xi, \psi \rangle_{\mathbb{I}(q)} = \langle \xi_Q(q), \psi_Q(q) \rangle_{M(q)} \tag{91}$$

Similar to above, this also induces a map $\mathbb{I}(q): \mathfrak{g}^{\text{rigid}} \rightarrow (\mathfrak{g}^{\text{rigid}})^*$ and an inner product $\langle \cdot, \cdot \rangle_{\mathbb{I}(q)^{-1}}$ on $(\mathfrak{g}^{\text{rigid}})^*$. We thus have the following commutative diagram, corresponding to (73):

$$\begin{array}{ccc} (\mathfrak{g}^{\text{rigid}}, \mathbb{I}(q)) & \xrightarrow{L(q)} & (T_q Q, M(q)) \\ \mathbb{I}(q) \downarrow & & \downarrow M(q) \\ ((\mathfrak{g}^{\text{rigid}})^*, \mathbb{I}(q)^{-1}) & \xleftarrow{L(q)^*} & (T_q^* Q, M(q)^{-1}) \end{array} \tag{92}$$

Note finally that we have the map $(\mathbb{I}(q)^{-1})^*: (\mathfrak{g}^{\text{rigid}})^* \rightarrow (\mathfrak{g}^{\text{rigid}})^{**} \cong \mathfrak{g}^{\text{rigid}}$, as we assume that $\mathfrak{g}^{\text{rigid}}$ is finite dimensional and hence reflexive.

The space of rigid body motions is now defined by

$$T_q^{\text{rigid}} Q = \text{range}(L(q)) \tag{93}$$

and so all of the rigid and shape subspaces are

$$T_q^{\text{rigid}} Q = \text{range}(L(q)), \quad T_q^{*, \text{rigid}} Q = M(q) \cdot T_q^{\text{rigid}} Q \tag{94a}$$

$$T_q^{\text{shape}} Q = (T_q^{\text{rigid}} Q)^\perp \cap T_q^{\text{fix}} Q, \quad T_q^{*, \text{shape}} Q = (T_q^{*, \text{rigid}} Q)^\perp \cap T_q^{*, \text{fix}} Q \tag{94b}$$

so that $T_q^{*, \text{shape}} Q = M(q) \cdot T_q^{\text{shape}} Q$. Observe that

$$(T_q^{*, \text{rigid}} Q)^\perp = \ker(L(q)^*) \tag{95}$$

The assumption that the admissible set function g is invariant under the action of G^{rigid} implies that $\langle dg(q), L(q)\xi \rangle = 0$ for all $\xi \in \mathfrak{g}^{\text{rigid}}$ and hence that $T_q^{\text{rigid}} Q$ is orthogonal to $T_q^{\text{norm}} Q$. Similarly, $\langle T_q^* h_q(u), L(q)\xi \rangle = 0$ for all $u \in T_0^* \mathbb{R}^3$ and $\xi \in \mathfrak{g}^{\text{rigid}}$, and so $T_q^{\text{nonfix}} Q$ is also orthogonal to $T_q^{\text{rigid}} Q$.

To compute the rigid body projection, we use (75) to see that

$$v_{\text{rigid}} = \mathbb{P}_{\text{rigid}}(v) = L(q)(\ell(q)^{-1})^* L(q)^* M(q)v \tag{96a}$$

$$p_{\text{rigid}} = \mathbb{P}_{*, \text{rigid}}(p) = M(q)L(q)(\ell(q)^{-1})^* L(q)^* p \tag{96b}$$

Finally, the shape projection operators are given by

$$v_{\text{shape}} = \mathbb{P}_{\text{shape}}(v) = (\mathbb{P}_{\text{fix}} - \mathbb{P}_{\text{rigid}})v \tag{97a}$$

$$p_{\text{shape}} = \mathbb{P}_{*, \text{shape}}(p) = (\mathbb{P}_{*, \text{fix}} - \mathbb{P}_{*, \text{rigid}})p \tag{97b}$$

7.7. Rigid-body momenta preservation

To ensure that the total linear and angular momentum of the system is preserved through the impact, it is important that the normal and frictional impulses introduce no net force or torque.

Friction is assumed to act only in the sliding direction, so we required in Section 4.4 that $I_{\text{slide}} \in T_q^{*, \text{slide}} Q$. This implies that the frictional impulse is orthogonal to the normal impulse, and also that it does not break the symmetry action of the group G^{rigid} , so the friction will not interfere with the conservation of angular and linear momentum. The general condition for I_{slide} to not break the symmetry is that

$$\langle I_{\text{slide}}, \zeta_Q(q_c) \rangle = 0 \quad \text{for all } \zeta \in \mathfrak{g}^{\text{rigid}} \tag{98}$$

(see, for example, Reference [10, Section 3.1.4]). Given the definition (94a) of $T_q^{*, \text{rigid}} Q$, we thus see that requirement (98) is exactly the same as requiring $I_{\text{slide}} \in (T_q^{*, \text{rigid}} Q)^\perp$. Clearly this is satisfied by requiring $I_{\text{slide}} \in T_q^{*, \text{slide}} Q$.

Recall furthermore that in (80), (95) and (84) we observed that $(T_q^{\text{norm}} Q)^\perp = \ker(\text{d}g(q))$, $(T_q^{*,\text{rigid}} Q)^\perp = \ker(L(q)^*)$ and $(T_q^{\text{nonfix}} Q)^\perp = \ker(T_q h_q)$, so that

$$\langle \text{d}g(q), v_{\text{slide}} \rangle = \langle \text{d}g(q), v_{\text{rigid}} \rangle = \langle \text{d}g(q), v_{\text{shape}} \rangle = 0 \quad (99a)$$

$$L(q)^*(p_{\text{norm}}) = L(q)^*(p_{\text{slide}}) = L(q)^*(p_{\text{shape}}) = 0 \quad (99b)$$

$$T_q h_q(p_{\text{rigid}}) = T_q h_q(p_{\text{shape}}) = 0 \quad (99c)$$

Here (99b) includes the statement that the normal impulse will not induce any rigid-body motions, while (99a) restates the fact that the sliding, rigid and shape velocities are non-normal, and (99c) shows that the rigid and shape momenta will not cause separation, interpenetration, or sliding.

8. CONCLUSIONS AND FUTURE DIRECTIONS

We derived a new explicit contact enforcement algorithm, termed decomposition contact response, starting from the conceptual non-smooth geometric mechanics framework. The overall algorithm is robust—it resolves the collisions between smooth and non-smooth bodies—and exhibits very good conservation properties in terms of linear and angular momentum as well as total energy. The closest point projections used for removing the interpenetrations introduce some spurious non-conservative effects, however these are minimal on the scale of the total momentum or energy of the system. As discussed, these effects can be further minimized by incorporating the work performed by the nodal forces during the projection into the energy balance.

In closing, a number of possible extensions of the theory are worth mentioning. Firstly, for bodies with smooth boundaries subdivision schemes [20] may be used for discretizing and parameterizing the contact surface. Although as demonstrated in the examples, simply the control mesh may be used for enforcing contact constraints. Proper treatment of smooth surfaces increases the fidelity of the contact stresses and forces as recently reported by several authors [24–26]. A further possible worthwhile future research direction is the study of convergence of the DCR method and in particular the interplay with the Newmark time-stepping scheme used here.

ACKNOWLEDGEMENTS

We are grateful to DoE for partial support through Caltech’s ASCI Center for the Simulation of the Dynamic Response of Materials (DOE W-7405-ENG-48, B523297). Special thanks to Sean Mauch, Center for Advanced Computing Research, Caltech, for providing the orthogonal range query software for contact search.

REFERENCES

1. Hallquist JO, Goudreau GL, Benson DJ. Sliding interfaces with contact-impact in large-scale Lagrangian computations. *International Journal for Numerical Methods in Engineering* 1985; **51**:107–137.

2. Wriggers P, Vu Van T, Stein E. Finite-element formulation of large deformation impact-contact problems with friction. *Computers and Structures* 1990; **37**:319–331.
3. Belytschko T, Lin JI. A three-dimensional impact-penetration algorithm with erosion. *Computers and Structures* 1987; **25**:95–104.
4. Belytschko T, Neal MO. Contact-impact by the pinball algorithm with penalty and Lagrangian methods. *International Journal for Numerical Methods in Engineering* 1991; **31**:547–572.
5. Carpenter NJ, Taylor RL, Katona MG. Lagrange constraints for transient finite-element surface-contact. *International Journal for Numerical Methods in Engineering* 1991; **32**:103–128.
6. Heinstein MW, Mello FW, Attaway SW, Laursen TA. Contact-impact modeling in explicit transient dynamics. *Computer Methods in Applied Mechanics and Engineering* 2000; **187**:621–640.
7. Belytschko T, Liu WK, Moran B. *Nonlinear Finite Elements for Continua and Structures*. Wiley: New York, 2000.
8. Laursen TA. *Computational Contact and Impact Mechanics*. Springer: Berlin, 2002.
9. Wriggers P. *Computational Contact Mechanics*. Wiley: New York, 2002.
10. Marsden JE, West M. Discrete mechanics and variational integrators. *Acta Numerica*, vol. 10. Cambridge University Press: Cambridge, MA, 2001.
11. Fetecau RC, Marsden JE, Ortiz M, West M. Nonsmooth Lagrangian mechanics and variational collision integrators. *SIAM Journal on Applied Dynamical Systems* 2003; **2**(3):381–416.
12. Aivazis M, Goddard WA, Meiron D, Ortiz M, Pool J, Shepherd J. A virtual test facility for simulating the dynamic response of materials. *Computing in Science and Engineering* 2000; **2**(2):42–53.
13. Kane C, Repetto EA, Ortiz M, Marsden JE. Finite element analysis of nonsmooth contact. *Computer Methods in Applied Mechanics and Engineering* 1999; **180**(1–2):1–26.
14. Pandolfi A, Kane C, Marsden JE, Ortiz M. Time-discretized variational formulation of non-smooth frictional contact. *International Journal for Numerical Methods in Engineering* 2002; **53**:1801–1829.
15. Fetecau RC, Marsden JE, West M. Variational multisymplectic formulations of nonsmooth continuum mechanics. In *Perspectives and Problems in Nonlinear Science*, Kaplan E, Marsden JE, Sreenivasan KR (eds). Springer: Berlin, 2003; 229–261.
16. Newmark NM. A method of computation for structural dynamics. *Journal of the Engineering Mechanics Division (ASCE)* 1959; **85**(EM3):67–94.
17. Kane C, Marsden JE, Ortiz M, West M. Variational integrators and the Newmark algorithm for conservative and dissipative mechanical systems. *International Journal for Numerical Methods in Engineering* 2000; **49**(10):1295–1325.
18. Laursen TA, Love GR. Improved implicit integrators for transient impact problems-geometric admissibility within the conserving framework. *International Journal for Numerical Methods in Engineering* 2002; **53**:245–274.
19. Goldsmith W. *Impact: The Theory and Physical Behaviour of Colliding Solids*. Edward Arnold Ltd.: London, 1960.
20. Cirak F, Ortiz M, Schröder P. Subdivision surfaces: a new paradigm for thin-shell finite-element analysis. *International Journal for Numerical Methods in Engineering* 2000; **47**(12):2039–2072.
21. Cirak F, Ortiz M. Fully C^1 -conforming subdivision elements for finite deformation thin-shell analysis. *International Journal for Numerical Methods in Engineering* 2001; **51**(7):813–833.
22. Cirak F, Scott MJ, Antonsson EK, Ortiz P, Schröder M. Integrated modeling, finite-element analysis and engineering design for thin-shell structures using subdivision. *Computer-Aided Design* 2002; **34**(2):137–148.
23. Abraham R, Marsden JE, Ratiu T. *Manifolds, Tensor Analysis, and Applications*. Applied Mathematical Sciences, (2nd edn), vol. 75. Springer: New York, 1988.
24. Puso MA, Laursen TA. A 3d contact smoothing method using gregory patches. *International Journal for Numerical Methods in Engineering* 2002; **54**:1161–1194.
25. Belytschko T, Daniel WJT, Ventura G. A monolithic smoothing-gap algorithm for contact-impact based on the signed distance function. *International Journal for Numerical Methods in Engineering* 2002; **55**:101–125.
26. Krstulovic-Opara L, Wriggers P, Korelc J. A C^1 continuous formulation for 3d finite deformation frictional contact. *Computational Mechanics* 2002; **29**:27–42.